INL/JOU-22-70328-Revision-0

Improved Multiphysics Model of the High Temperature Test Reactor for the Simulation of Loss of Forced Cooling Experiments

September 2023

Vincent M Laboure, Javier Ortensi, Nicolas Pierre Martin, Paolo Balestra,
Derek R Gaston, Yinbin Miao, Gerhard Strydom

INL/JOU-22-70328-Revision-0

Improved Multiphysics Model of the High Temperature Test Reactor for the Simulation of Loss of Forced Cooling Experiments

Vincent M Laboure, Javier Ortensi, Nicolas Pierre Martin, Paolo Balestra, Derek R Gaston, Yinbin Miao, Gerhard Strydom

September 2023

Idaho National Laboratory
Idaho Falls, Idaho 83415

http://www.inl.gov

Prepared for the
U.S. Department of Energy
Under DOE Idaho Operations Office
Contract DE-AC07-05ID14517, DE-AC07-05ID14517

Improved Multiphysics Model of the High Temperature Engineering Test Reactor for the Simulation of Loss-of-Forced-Cooling Experiments

Vincent Labouré,*,[a] Javier Ortensi,[a] Nicolas Martin,[a] Paolo Balestra,[a] Derek Gaston,[a] Yinbin Miao,[b] and Gerhard Strydom[a]

[a] *Nuclear Science and Technology Directorate*
Idaho National Laboratory
P.O. Box 1625
Idaho Falls, ID 83415

[b] *Chemical and Fuel Cycle Technologies Division*
Argonne National Laboratory
9700 South Cass Avenue
Lemont, IL 60439

*Email: vincent.laboure@inl.gov

Number of pages:	49
Number of tables:	7
Number of figures:	23

Abstract

We present a multiphysics model of the High Temperature Engineering Test Reactor for comparison with past and predict future loss-of-forced-cooling (LOFC) experiments. The approach selected combines (1) 3-D full-core superhomogenization-corrected neutronics, (2) 3-D full-core homogenized or semi-heterogeneous heat transfer (macroscale), (3) 2-D axisymmetric fuel rod heat transfer (pin-scale), and (4) 1-D thermal-hydraulics channels. Although large uncertainties remain, the time and magnitude of the first power peak after re-criticality is predicted within 1.5 hours and 175 kW, respectively. The novelty of our work includes (1) a new macroscale/pin-scale heat transfer coupling approach relying on gap conductance to drastically speed up numerical convergence by two orders of magnitude, (2) determination of a radial effective thermal conductivity, reproducing the semi-heterogeneous re-criticality time within one hour using a homogenized macroscale model, and (3) a preliminary study of the reactor's early behavior following a LOFC event, enabling further assessment of numerical models against fission power measurements.

Keywords — Multiscale Heat Transfer Coupling, Effective Thermal Conductivity, Reactor Physics Analysis, High Temperature Engineering Test Reactor, Loss-of-Forced Cooling

I. INTRODUCTION

The High-Temperature Engineering Test Reactor (HTTR) is a helium-cooled, graphite-moderated prismatic reactor operated by the Japan Atomic Energy Agency (JAEA). It was designed to aid in safety analyses of high-temperature gas-cooled reactors (HTGRs) [1]. It conducted many experimental tests from 1998 to 2011, at which point it was shut down following the Fukushima accident, before being restarted in 2021. Of particular interest are three loss-of-forced-cooling (LOFC) tests, classified as anticipated transients without scram, for which JAEA has either provided or will be providing experimental data to participating countries under the Civil Nuclear Energy Research and Development Working Group. Such data are invaluable for the validation of codes targeting HTGRs as well as gas-cooled microreactors, given HTTR's low thermal rated power of 30 MW. The data from the first experiment, performed at 9 MW and with the vessel cooling system (VCS) operating, were already provided, whereas the data from the next two experiments—at 30 MW and then at 9 MW, with the VCS turned off—should become available in the near future (the former has yet to be completed; the latter was performed recently, but the corresponding experimental data have not yet been provided).

To accurately simulate such unprotected LOFC events and predict the maximum temperatures reached, as well the time at which the reactor again reaches criticality (i.e., the *re-criticality time*), followed by the subsequent power evolution, many key phenomena must be appropriately modeled. These include decay heat, neutron poison evolution, and heat removal by conduction, convection, and radiation [2]. Thus, numerical simulations require a multiphysics approach coupling neutronics, heat transfer, and thermal-hydraulics. In other works, many different approaches have been considered for each of these physics. For the neutronics component, prismatic HTGR models for LOFC simulations include solvers that rely on block-wise point kinetics [2], 2-D axisymmetric (R-Z) diffusion codes [3], or spherical harmonics (PN) hybrid finite element [4]. For the conjugate heat transfer, ring models with system codes [5, 4], a 2-D R-Z full-core heat conduction model with few flow channels [2] or porous media flow models [3, 6], as well as computational fluid dynamics [7, 8] have been previously considered, as summarized in [9]. High-fidelity calculations for each physics—as performed in [10, 11]—could constitute another attractive approach if they can be efficiently extended to transient calculations.

Historically, our approach has been to target the resolution of 3-D effects for both the neutronics and heat transfer phenomena at the full-core level. Specifically, our previous models used (1) 3-D full-core superhomogenization (SPH)-corrected neutronics, (2) 3-D homogenized full-core heat transfer, (3) one representative 2-D R-Z heterogeneous rod per fuel block, and (4) one 1-D representative thermal-hydraulics channel per fuel and control rod (CR) column [12, 13, 14, 15]. In this work, we address several important deficiencies of the model in terms of numerical performance and how well it compared to experimental results:

1. The 3-D full-core heat transfer model (henceforth referred to as the *macroscale* model) relied on a homogeneous mesh, but determination of an effective thermal conductivity was lacking. In this work, we consider a 2-D *semi-heterogeneous* macroscale model that represents the graphite blocks heterogeneously but excludes fuel rods and cooling channels, and we predict an effective thermal conductivity by imposing a heat flux on the boundary of the fuel cooling channels, along with a temperature at the radial periphery of the permanent reflector. We then compare two macroscale approaches for the LOFC simulation: one using a 3-D homogenized model with effective thermal conductivity, and another directly using a 3-D semi-heterogeneous model, yielding reasonably close results but with the computational cost differing by a factor of 5 or more.

2. The coupling between the macroscale model and the 2-D axisymmetric rod-wise model (henceforth referred to as the *pin-scale* or pin-level heat transfer model) exhibited poor numerical stability, thereby drastically constraining the maximum time step size and leading to an extremely slow convergence of the steady-state solution. We propose what is, to the best of our knowledge, a novel approach—one that can be applied to either the homogenenous or semi-heterogeneous macroscale model—relying on heat transfer coefficients (HTCs) for convection and gap conductances in order to model both conduction and radiation heat transfer, and reducing the cost of the steady-state simulation by about two orders of magnitude. An alternative strategy that was successfully developed for other reactors [16] is to combine the macroscale and pin-level heat transfer models into a single heterogeneous heat transfer model, but because this considerably increases the computational resources required, it is not currently considered in this work.

3. The LOFC simulation results from our previous models exhibited an additional early recriticality (i.e., within 30 minutes of the initial event—not many hours later, as had been

expected) absent in the experimental data [14]. It is not entirely clear whether models from other institutions contained similar defects, because the early fission power behavior was, to our knowledge, never closely studied, though results from [2] suggest it was at least observed (see Section III.C). Thus, the third goal of this work is to investigate which parameters can affect predictions of such a re-criticality—namely, temperature feedback coefficients and parameters affecting rod-wise heat transfer. More generally, we believe that this early behavior is worthy of attention, as it could be utilized to further validate the codes by using the limited amount of publicly available experimental data. Indeed, most of the data available pertain to the LOFC fission power evolution and ex-core temperature, which are both susceptible to error compensation.

The remainder of this paper is organized as follows: first, we give an overview of the numerical model in Section II. Next, we propose and study improvements to the model in Section III which constitute the novelty of this work. Section III.A presents the novel coupling approach applicable to the homogeneous and semi-heterogeneous macroscale models, Section III.B describes the methodology for deriving the effective thermal conductivity for the homogenized macroscale model, and Section III.C explores the fission power's early behavior. Finally, we present the post-experiment (9 MW) and pre-experiment (30 MW) LOFC simulation results in Section IV, and draw our conclusions in Section V.

II. OVERVIEW OF THE NUMERICAL MODEL

Fig. 1(a) shows the general layout of the core, with 30 fuel, 16 CRs, 12 replaceable reflectors, and three instrumentation columns, surrounded by a cylindrical permanent reflector (PR). Each column is composed of nine blocks, 58 cm in height, with the top and bottom two constituting the axial reflectors. The fuel enrichments and burnable poisons inside the fuel blocks vary both axially and radially, as summarized in Fig. 1(b). The cold helium flows upward between the reactor pressure vessel (RPV) and PR, then downward via the cooling channels inside the core. The VCS serves as the ultimate heat sink during LOFC conditions, with the heat from the RPV being transferred to it primarily through radiation and natural circulation [2].

We now present an overview of the base numerical model that we worked to improve upon. A summary of the simulation workflow is provided in Fig. 2: cross sections were first prepared with

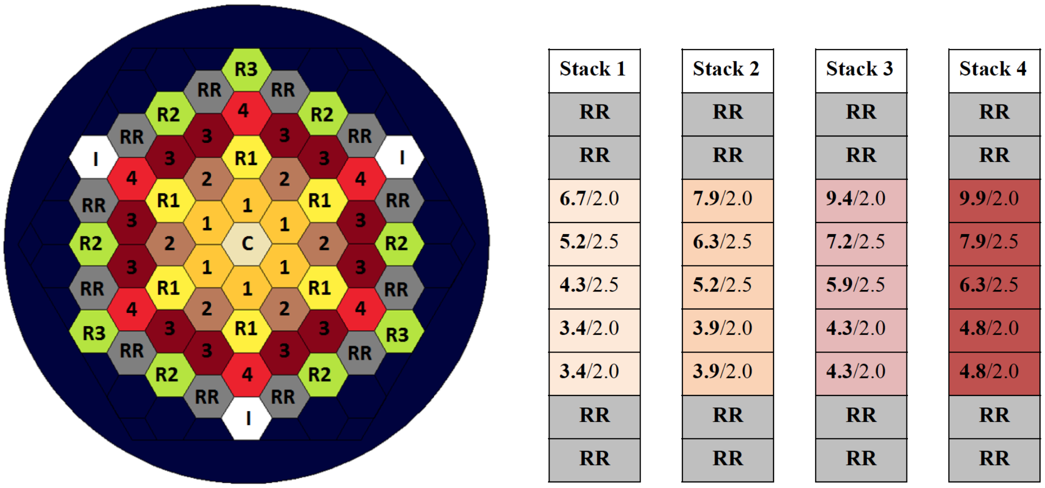

Stack 1	Stack 2	Stack 3	Stack 4
RR	RR	RR	RR
RR	RR	RR	RR
6.7/2.0	**7.9**/2.0	**9.4**/2.0	**9.9**/2.0
5.2/2.5	**6.3**/2.5	**7.2**/2.5	**7.9**/2.5
4.3/2.5	**5.2**/2.5	**5.9**/2.5	**6.3**/2.5
3.4/2.0	**3.9**/2.0	**4.3**/2.0	**4.8**/2.0
3.4/2.0	**3.9**/2.0	**4.3**/2.0	**4.8**/2.0
RR	RR	RR	RR
RR	RR	RR	RR

(a) HTTR core layout with fuel (columns 1–4), control rods (C, R1, R2, R3), replaceable reflectors (RR), and instrumentation (I).

(b) Description of the four different HTTR fuel columns/stacks (UO_2 wt% fuel enrichment / burnable poison wt% enrichment).

Fig. 1. Overall depiction of the HTTR model. Pictures courtesy of [12].

Monte Carlo, then corrected via a superhomogenization (SPH) procedure. Afterward, the coupled multiphysics multiscale model was used to solve a steady-state problem in order to provide the initial condition for the transient LOFC simulation.

The multiphysics simulations were performed using Sabertooth, which consists of the following Multiphysics Object-Oriented Simulation Environment (MOOSE)-based applications: Griffin [17, 18] for neutronics, the heat conduction MOOSE module and BISON [19] for heat transfer, and RELAP-7 [20] for thermal-hydraulics. The primary motivation for selecting the individual codes was that they were designed to simulate the physics of interest while being built upon the MOOSE framework—which facilitates their multiphysics coupling. Other tools could be considered in the future, such as SAM [21] or Pronghorn [22] which are specifically designed for single phase system analysis and porous media modelling, respectively.

We now give a summary of each model. This presentation is not meant to be exhaustive, since a very detailed examination of the models and assumptions can already be found in [15].

II.A. Neutronics

For the Griffin neutronics model, we applied the traditional two-step approach by generating cross sections for various core conditions before using them in the multiphysics model for both

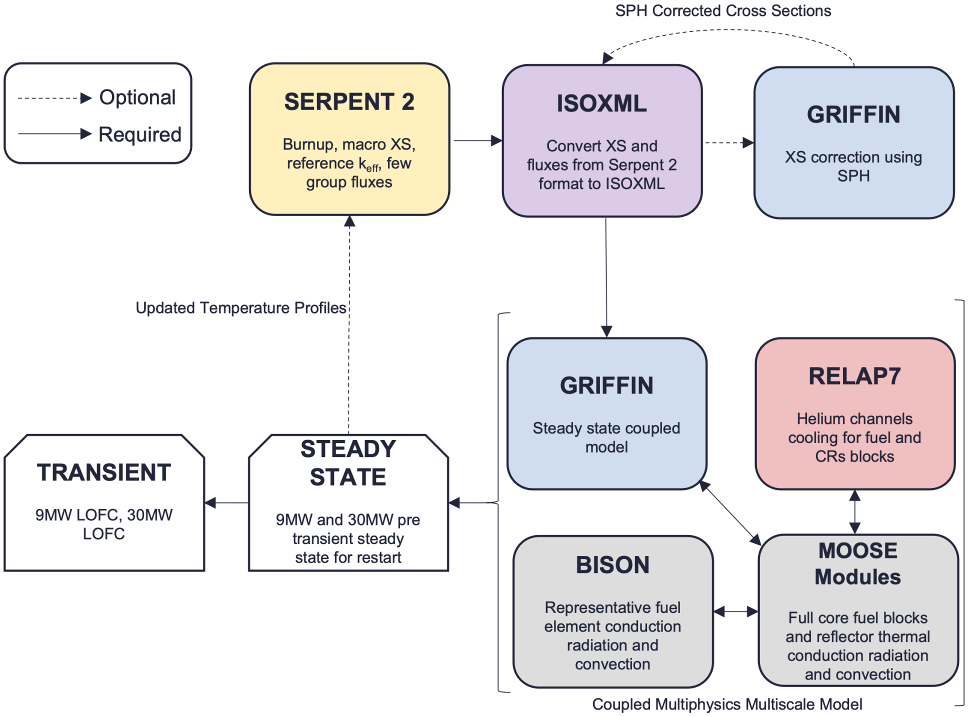

Fig. 2. Overview of the simulation workflow.

the steady-state and transient calculations. More specifically, we first depleted a full-core Serpent [23] model up to a burnup level representative of when the LOFC experiments were—or are to be—completed (i.e., at around 373 effective full-power days [EFPDs]). We then performed branch calculations by varying the average fuel and moderator temperatures (i.e., $\overline{T}_{\text{fuel}}$ and $\overline{T}_{\text{mod}}$, respectively), while maintaining the axial temperature profiles (determined via a previous version of this multiphysics model) to generate a tabulated multigroup cross-section library [12], using the energy group structure shown in Table I. Note that, although the full-core SPH procedure guarantees an accurate power distribution at state points, the choice of group structure can affect kinetics parameters [24]. The present one was studied in [25] and compared against experimental data from the graphite-moderated TREAT reactor, though it may warrant further study. In [15], the Serpent model compared fairly well against previous benchmark calculations as well as experimental results, including in regard to such values as excess reactivity, axial neutron flux distribution, shutdown margin, and axial and radial power distributions.

The evolution of the concentration of the main neutron poison of interest (i.e., Xe-135) during the experiment was explicitly modeled using the poison tracking capability in Griffin. To achieve this, its contribution to the macroscopic cross sections was first removed from the multigroup library, and the concentrations of Xe-135 and its precursor, I-135, were explicitly tracked during the transient by using the microscopic absorption cross sections and effective fission yields computed by Serpent.

In parallel, a 3-D full-core homogeneous mesh (see Fig. 3) was created using the Neutronics Enhanced Meshing Operations (NEMO) software [26], which interfaces with Cubit [27] and adds flux detectors to the Serpent input. These reference fluxes were then utilized by the full-core SPH equivalence procedure within Griffin [28] in order to reproduce, at each state point, the reactor multiplication factor, power density distribution, and integrated leakage out of the SPH-corrected regions (provided that all the fuel regions have been corrected for), as proven in [29]. In practice, for all state points considered in this work, the reference Serpent eigenvalue is reproduced by Griffin to within 10^{-5} pcm, and the maximum absolute relative error in power for any SPH region is below 10^{-8}. The high level of integration between Griffin, Serpent and NEMO was the primary motivation for selecting Serpent for cross-section and reference fluxes generation.

TABLE I
Energy group upper boundaries for the 10-group structure from [12] used in the neutronics model.

Group	Energy (MeV)	Group	Energy (MeV)
1	2.0010E-08	6	8.1000E-06
2	4.7302E-08	7	1.3270E-04
3	7.6497E-08	8	3.4811E-03
4	2.0961E-07	9	1.1562E-01
5	6.2500E-07	10	4.0000E+01

The multigroup cross-section library was then tabulated with respect to $\overline{T}_{\text{mod}}$ and $\overline{T}_{\text{fuel}}$, expressed in K, with:

- $\overline{T}_{\text{fuel}} \in \{450, 550, 650, 750, 850\}$ and $\overline{T}_{\text{mod}} \in \{400, 500, 600, 700, 800\}$ for the 9 MW case
- $\overline{T}_{\text{fuel}} \in \{800, 950, 1100, 1250, 1400, 1550\}$ and $\overline{T}_{\text{mod}} \in \{500, 650, 800, 950, 1100, 1250\}$ for the 30 MW case.

The corresponding fuel and moderator temperature reactivity coefficients are reported in Table II.

Because the LOFCs of interest are unprotected transients, another key aim of the neutronics model is to account for the three Cf-252 fixed neutron sources present in HTTR. Indeed, the reactor remains in a sub-critical state for many hours after the initial event, and thus the flux levels shortly

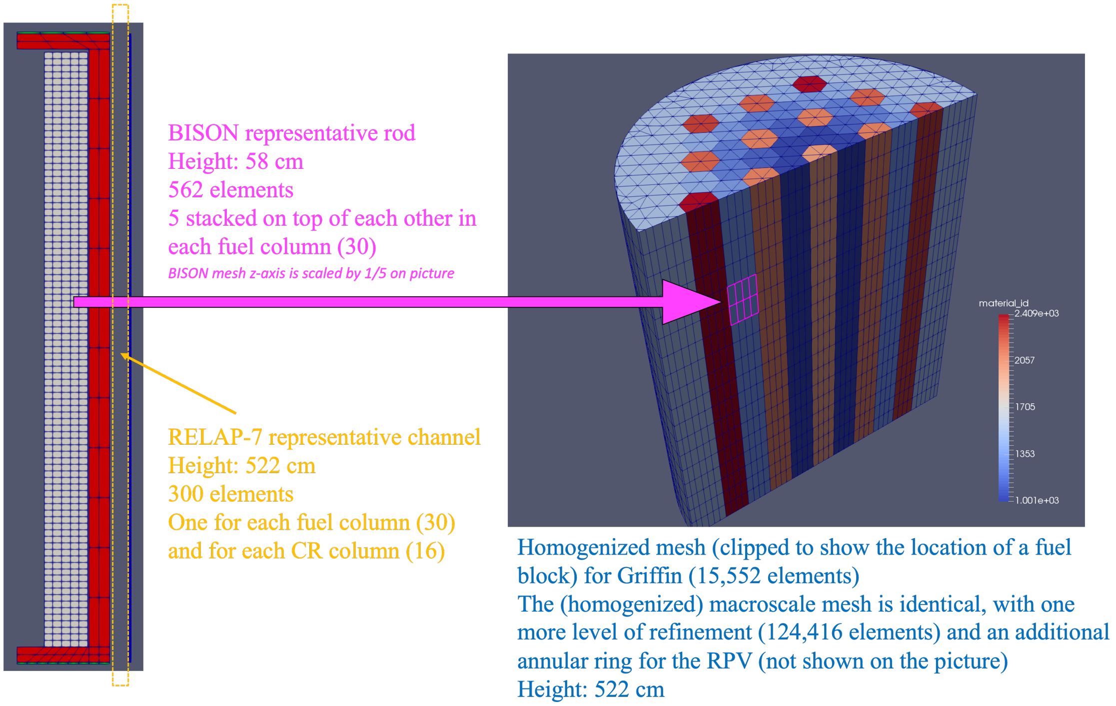

Fig. 3. Interrelation of the various sub-models and their meshes via a homogeneous macroscale model. For the semi-heterogeneous macroscale model, the macroscale mesh is given in Fig. 8.

before re-criticality are primarily driven by the intensity of these sources, thus noticeably impacting the rest of the transient [2]. Given the half-life of Cf-252 (2.645 years), the three 3.7 GBq sources must be replaced every 7 years [30].

To convert the rate of Cf-252 disintegrations into a neutron source, the following formula is used:

$$S = Q\,\gamma_{\mathrm{SF}}\,\nu\exp(-\ln(2)t/\tau), \tag{1}$$

where $Q = 3.7 \times 10^9$ s^{-1} is the initial Cf-252 disintegration rate of a single source, $\gamma_{\mathrm{SF}} = 3.09\%$ is the Cf-252 spontaneous fission probability, ν is the number of neutrons emitted per spontaneous fission event (assumed to be 3.77 [31]), t is the age of the source, and τ is the Cf-252 half-life.

The energy spectrum, $\mathcal{P}$, of the neutrons emitted by such events is also needed. Assuming that the spontaneous neutron spectrum is similar to that of a fission reactor [32], and that it can be modeled using the empirical Watt distribution for U-235 fission [33]:

$$\mathcal{P}(E) = a\sinh(\sqrt{2E/E_0})\exp(-E/E_0), \tag{2}$$

TABLE II
Fuel and moderator temperature reactivity coefficients (α_f and α_m, respectively) in pcm/K, as obtained from the 9 and 30 MW libraries.

9 MW Library				30 MW Library			
$\overline{T}_{\text{fuel}}$	$\overline{T}_{\text{mod}}$	α_f	α_m	$\overline{T}_{\text{fuel}}$	$\overline{T}_{\text{mod}}$	α_f	α_m
450	400			800	500		
450	500		-5.94	800	650		-4.05
450	600		-5.96	800	800		-3.90
450	700		-5.77	800	950		-3.57
450	800		-5.15	800	1100		-3.57
550	400	-6.54		800	1250		-3.31
550	500	-6.32	-5.71	950	500	-5.14	
550	600	-6.06	-5.71	950	650	-4.90	-3.81
550	700	-5.93	-5.64	950	800	-4.77	-3.77
550	800	-5.74	-4.97	950	950	-4.59	-3.38
650	400	-6.34		950	1100	-4.51	-3.50
650	500	-6.03	-5.39	950	1250	-4.50	-3.31
650	600	-5.90	-5.58	1100	500	-4.76	
650	700	-5.69	-5.43	1100	650	-4.53	-3.59
650	800	-5.63	-4.91	1100	800	-4.35	-3.59
750	400	-6.21		1100	950	-4.26	-3.30
750	500	-6.00	-5.18	1100	1100	-4.14	-3.38
750	600	-5.71	-5.29	1100	1250	-4.09	-3.26
750	700	-5.52	-5.24	1250	500	-4.63	
750	800	-5.40	-4.79	1250	650	-4.39	-3.35
850	400	-5.89		1250	800	-4.26	-3.46
850	500	-5.60	-4.89	1250	950	-4.15	-3.19
850	600	-5.42	-5.11	1250	1100	-4.04	-3.26
850	700	-5.27	-5.09	1250	1250	-3.96	-3.18
850	800	-5.16	-4.67	1400	500	-4.31	
				1400	650	-4.14	-3.17
				1400	800	-3.94	-3.27
				1400	950	-3.81	-3.05
				1400	1100	-3.77	-3.23
				1400	1250	-3.78	-3.19
				1550	500	-4.29	
				1550	650	-4.14	-3.02
				1550	800	-3.97	-3.09
				1550	950	-3.91	-2.99
				1550	1100	-3.80	-3.12
				1550	1250	-3.78	-3.17

where E is the energy (in MeV) of the emitted neutrons, $E_0 = 1$ MeV, and $a \approx 0.48$ MeV^{-1} is chosen such that:

$$\int_0^\infty \mathcal{P}(E)\mathrm{d}E = 1. \tag{3}$$

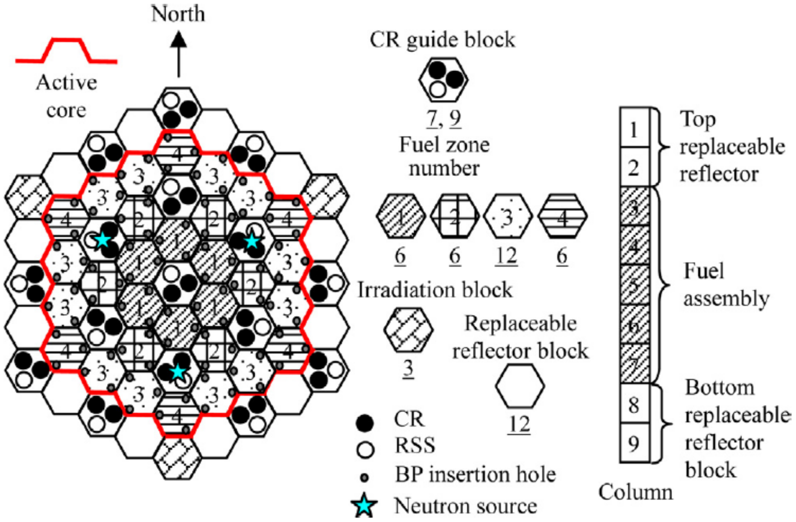

Fig. 4. Visualization of the location of the neutron sources. (Figure courtesy of [2].)

The fixed volumetric source corresponding to the group of index g is then defined as:

$$q_g = \frac{S}{V_{\text{block}}} \int_{E_{g+1}}^{E_g} \mathcal{P}(E)\mathrm{d}E, \tag{4}$$

where $V_{\text{block}} \approx 0.0651$ m^3 is the total volume of a (homogenized) block.

Based on the supposed replacement dates, we estimate, in Table III, the intensity of the volumetric source applied in the three blocks shown with a blue star in Fig. 4, in the first layer of fuel underneath the top axial reflector (axial index 3). It is only applied during the transient, since an eigenvalue calculation with a fixed source has no solution. This is non-problematic because the volumetric source at the beginning of the transient is completely negligible.

TABLE III

Intensity of the homogenized neutron source in each energy group in 1/(m^3-s).

	Estimated source age (yrs)	$g = 1$	$g = 2$	$g = 3$	$g = 4 - 10$
LOFC #1 (9 MW)	4	2.2812E+09	3.9730E+07	2.1548E+05	0
LOFC #2 (30 MW)	6	1.3506E+09	2.3523E+07	1.2758E+05	0

In terms of decay heat, we used Serpent to generate the total decay power as a function of time by assuming a zero flux after the loss of cooling, then distributed it in the homogenized fuel blocks proportionally to the steady-state fission power distribution.

II.B. Thermal-Hydraulics

To greatly simplify the thermal-hydraulics model, we considered independent channels extending from the top of the upper axial reflector to the bottom of the lower axial reflector. Specifically, a single representative channel for each of the 30 fuel columns (1–4 in Figure 1(a)) and 16 CR columns (C, R1, R2, and R3 in Figure 1(a)) was simulated. In addition, the flow in the inter-column gaps was neglected, and the bypass flow, defined as the proportion of the total mass flow rate skirting the fuel cooling channels, was set to a constant value of $\alpha = 8\%$, as was the case in [3]. In each cooling channel type, the total corresponding mass flow rate was divided equally across all the channels.

For the thermal-hydraulics model, we considered 46 independent RELAP-7 channels, with a downward helium flow over the height of the core: one representative cooling channel for each of the 30 fuel columns and 16 CR columns, as illustrated in Fig. 5. Both use 300 1-D elements. First, the CR channels were modeled as tubes featuring a constant diameter of 123 mm over the entire height of the core. This simplification ignores the fact that some CRs should be partially inserted, or that the 9 and 30 MW cases require insertions at different positions (this is, however, appropriately modeled in the Serpent input) [34]. Second, for the fuel channels, helium enters a cylinder whose outer diameter is 41 mm, goes around an inner cylinder whose diameter is 34 mm (representing the graphite sleeves) over the height of the fuel blocks (excluding the top and bottom axial reflectors), then recombines at the bottom axial reflector.

The HTCs during the steady-state calculation are automatically computed by RELAP-7, using closures specifically derived for HTGRs [35].

It is not clear what flow pattern is established during the LOFC experiments, as information obtained from the literature appears contradictory. For example, [36] describes a residual flow amounting to 0.3% of the nominal mass flow rate persisting throughout the transient, stemming from the helium purification system. In addition, the JAEA experimental data exhibit an inlet temperature consistently lower than the outlet temperature at the bottom of the core, generally indicating that forced convection is still happening. Nevertheless, another publication by JAEA, published several years after the 9 MW test, makes no mention of this residual flow, and only speaks of natural circulation with flow reversal [2]. In the absence of a clear understanding, we assumed that the cooling channels no longer removed heat during the LOFC simulations. While

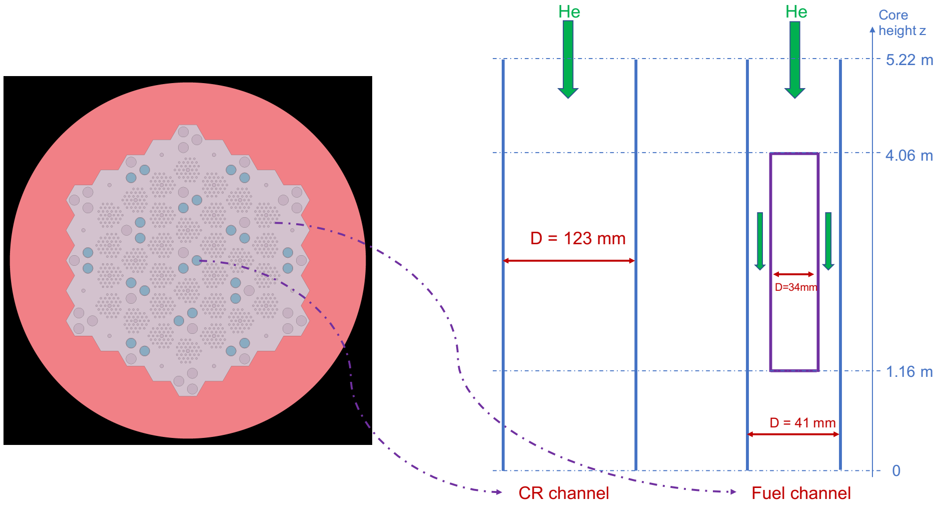

Fig. 5. Left: cross-section view of the Serpent model. Right: description of the RELAP-7 models for fuel and CR channels. Figure courtesy of [13].

this is a significant assumption, we emphasize that it is independent of the model improvements studied in Section III.

II.C. Macroscale Heat Transfer

The macroscale model was designed to simulate the 3-D transfer of heat at the full-core level. This model is supposed to calculate the heat exchange between the fuel rods, cooling channels, graphite blocks, graphite PR, stainless-steel RPV[a], and the VCS, which is modeled through boundary conditions (BCs). (The temperature of the VCS is assumed to remain constant at 300 K during the steady state and LOFC simulations). Two strategies were considered in regard to modeling the graphite blocks: a homogeneous and a semi-heterogeneous approach.

II.C.1. Homogeneous Model

This model, illustrated in Fig. 6, represents all the graphite blocks and the holes within them as a porous medium, with adjusted density. The mesh itself is identical to the neutronics mesh, as detailed in Fig. 3, with an additional level of uniform refinement and the RPV meshed. An anisotropic effective thermal conductivity model is derived in Section III.B. All in-core heat source and sink terms that result from radiation, convection, and conduction from the fluid and the fuel

---

[a] Note that we do not currently model the components between the PR and RPV (e.g., the side shielding blocks).

were applied as volumetric terms, as detailed in Section III.A.3. In particular, the convection terms were applied as the following volumetric source:

$$q''' = \widetilde{h}_{\text{outer}}\left(T - T_{\text{fluid}}\right), \tag{5}$$

where T_{fluid} is the block-averaged fluid temperature and $\widetilde{h}_{\text{outer}}$ is the volumetric outer-wall HTC (in W/K/m^3):

$$\widetilde{h}_{\text{outer}} = \frac{\pi D n_{\text{rods}}}{S_{\text{block}}} h_{\text{outer}}, \tag{6}$$

where h_{outer} is the block-averaged outer-wall HTC, n_{rods} is the number of fuel rods or CR holes in the block, D is the outer diameter of the hole, and S_{block} is the cross-sectional area of the (homogenized) graphite blocks ($S_{\text{block}} = \sqrt{3}p^2/2$, with p being the width across flats). The terms due to radiation and conduction will be similarly constructed in Section III.A.

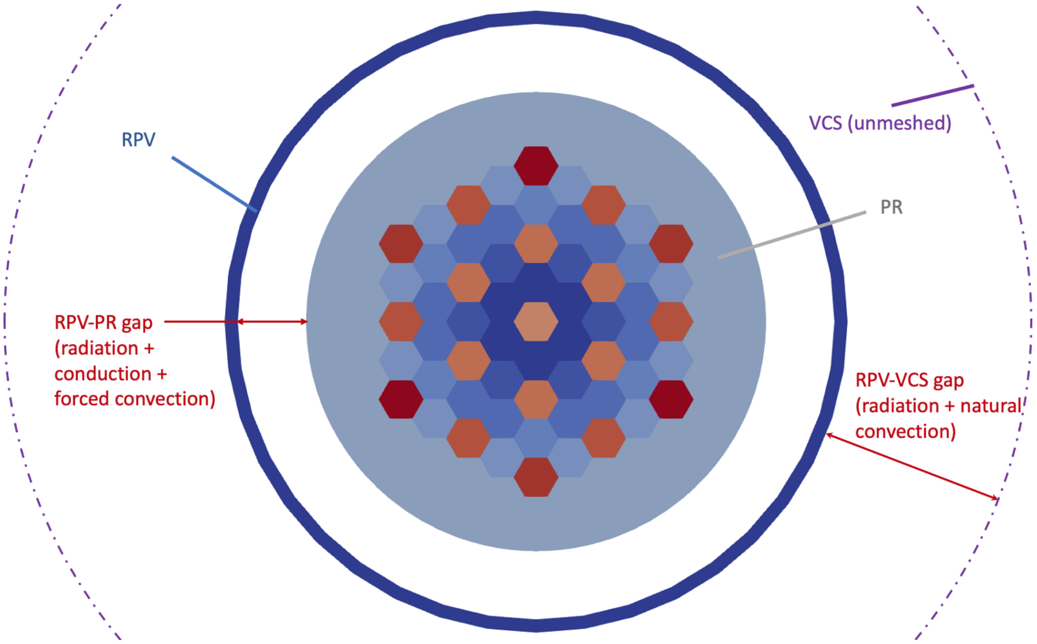

Fig. 6. Clipped view of the 3-D homogeneous macroscale heat transfer model. The dark purple circle represents the VCS, only modeled through boundary conditions. (Figure courtesy of [15].)

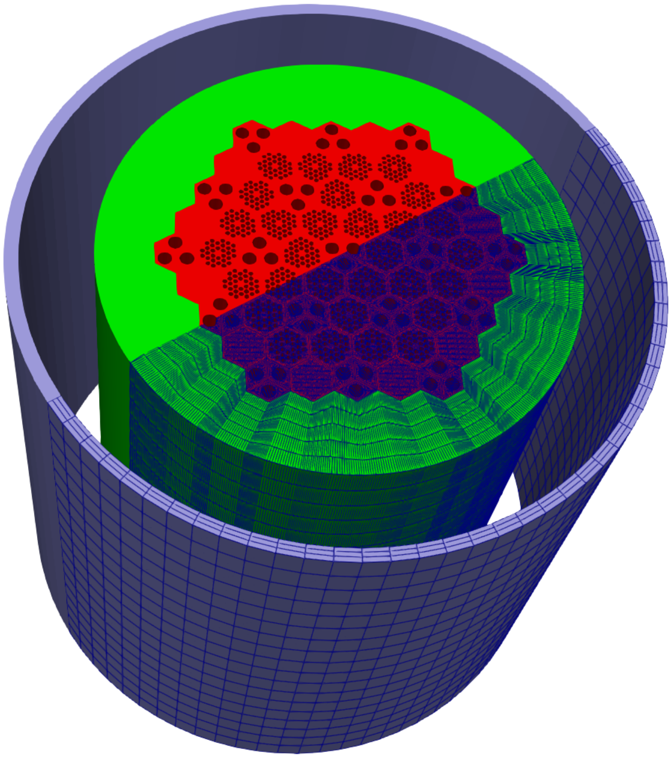

Fig. 7. Semi-heterogeneous mesh (651,240 elements) for the macroscale heat transfer model. To enable better visualization of the details, only half the mesh displays the actual elements.

II.C.2. Semi-heterogeneous Model

The second option considered in this work is to explicitly mesh the graphite blocks and exclude the embedded fuel and CR cooling channels. We used the MOOSE reactor module to create the mesh shown in Fig. 8 [37], and applied all in-core heat source and sink terms as surface terms (i.e., BCs).

II.D. Pin-Level Heat Transfer

The pin-level heat transfer model consists of one 2-D axisymmetric rod per fuel block, as shown on the left in Fig. 3. Each rod is composed of an annular fuel compact (in grey in Fig. 3) surrounded by a graphite sleeve (in red in that same figure), and is separated from the graphite block by the cooling channel (unmeshed). The block-averaged power density computed by the neutronics model is scaled and applied to the fuel compact. Heat can then dissipate via conduction as a result of direct contact between the fuel compact and the sleeve. In addition, radiation and conduction through gaps are modeled between the fuel compact and the sleeve (axially and radially), as well as through the cooling channel. At the radial periphery of the mesh (on the outer side of the cooling channel), the block- or surface-averaged (within a given block) solid temperature computed by the macroscale model is applied if the macroscale model is homogeneous or semi-heterogeneous, respectively. In both cases, we impose it via a pseudo-Dirichlet BC (i.e., using a Robin BC with a very large HTC that acts as a penalty factor), as was originally done in [38], so as not to degrade the global energy balance of the pin-scale model. Given the long time scale characterizing a LOFC event, the TRISO particles are assumed in quasi-thermal equilibrium with the fuel compact and the fuel temperature is computed as the average fuel compact temperature. Future work will assess the impact of this assumption.

II.E. Multiscale Multiphysics Coupling

We coupled the neutronics, heat transfer, and thermal-hydraulics models by using the MOOSE `MultiApp` system [39]. For the steady-state calculation, the neutronics input solves an eigenvalue problem for the scalar fluxes, with additional steady-state equations for the poison tracking. After each solve, the power density is passed to the other applications, which solve a *pseudo-transient* (i.e., a transient problem until a thermal equilibrium is reached). There are two main reasons for this approach: (1) certain applications such as RELAP-7 can only solve time-dependent problems, and (2) numerical convergence and stability can be drastically degraded if the macroscale heat transfer time derivative terms are omitted [13]. (Note, however, that omitting the time derivative terms of the pin-scale model is acceptable, and is used in this step of the model.) Once the pseudo-transient is completed, moderator and fuel temperatures are passed back to the neutronics, and this Picard iteration process is repeated until the desired convergence criteria are met. For the LOFC calculations, the thermal-hydraulics is skipped (as described in Section II.B), and all the other applications directly solve transient problems by applying two levels of Picard iterations (one between the neutronics and the macroscale models, and one between the macroscale, pin-scale, and thermal-hydraulics models).

The data transfer process, summarized in Figure 8, is complicated by the fact that the model combines 3-D Cartesian homogenized or semi-heterogeneous, 2-D axisymmetric heterogeneous, and 1-D meshes. To attain reasonable energy conservation, most transfers between the macroscale

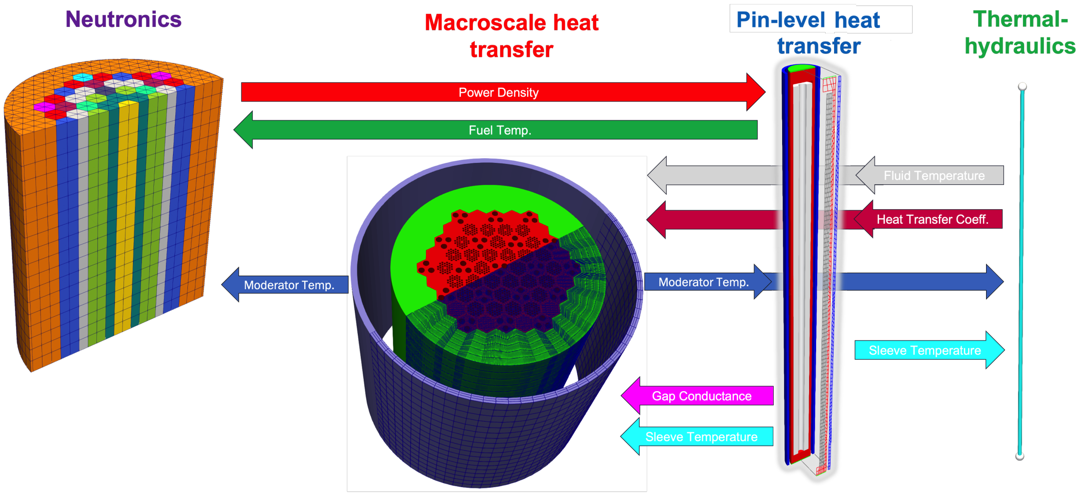

Fig. 8. Data transfer in steady state simulations. For the transient calculations, the transfers to and from the thermal-hydraulics model are omitted.

model and the pin-scale and thermal-hydraulics models are performed by computing the desired quantities in each block (i.e., in each axial layer and each fuel or CR column).

The data transfer to the macroscale heat transfer model differs from that seen in previous works in which we relied on heat fluxes from the pin-scale model [14], and will be discussed in detail in Section III.A.

III. MODEL IMPROVEMENTS

We now present the main novel improvements that were made to the model and that could potentially extend beyond this particular problem.

III.A. Multiscale Heat Transfer Coupling

III.A.1. Rationale

A previous model (e.g., in [14]) computed the heat flux coming through the outer boundary of the fuel cooling channels (at the pin level), and applied that heat flux as a volumetric source in the homogenized macroscale model. Unfortunately, this led to poor numerical stability of the steady-state solver. The underlying reason for this is because, during a macroscale solve, the coupling terms coming from the pin-level heat transfer model remain unchanged—since they are only updated once per Picard iteration—and thus the amount of heat added by the sources (whether volumetric or surfacic) is proportional to the time step size, Δt. Therefore, if a given location close to these sources is far from thermal equilibrium (e.g., because the transferred heat flux is not yet converged), the temperature field can drastically change if Δt is large. In fact, this is the very observation that motivated the use of pseudo-transients in [13] in lieu of steady-state calculations (which correspond to the limit $\Delta t \to \infty$). Here, we emphasize that even with a pseudo-transient, the transfer of heat fluxes—at least in the context of a fixed-point iteration strategy—tends to limit the maximum allowable time step during the pursuit of steady-state solutions. For this reason, the steady-state problem of the model described in [14] was very slow to converge (48 hours using 48 processors were not sufficient to fully converge the solution). A similar motivation led to the selection of (Robin) convective BCs over Neumann BCs in [40]. Indeed, convective-like terms do not act as a constant source, since their intensity changes with variations in local temperature (see Eq. 5). In similar fashion, a fully heterogeneous heat transfer approach (i.e., combining the macroscale and pin-level heat transfer models into one fully detailed, full-core model) with convective-based coupling to thermal-hydraulics was used in [16], without sparking any convergence issues.

Nevertheless, we estimated that the fully heterogeneous approach was not easily achievable given the detailed geometry at the rod level, as it likely would have resulted in a mesh with tens of millions of elements, thus significantly slowing down the calculation. Therefore, we are retaining the macroscale/pin-scale approach. This approach may remain appealing regardless, considering the reduced cost of the simulation—especially for cores even bigger than HTTR.

Our first attempt was to define an equivalent HTC, as was done in [40], to model heat transfer via convection, conduction, and radiation between the macroscale and pin-scale, but our effort was unfruitful because this HTC did not have any physical meaning and could thus become negative or arbitrarily large (often leading to unphysical solutions). The breakthrough came when we realized that heat transfer through a small gap (via conduction and radiation) behaves as a convective term—the equivalent of the HTC being the gap conductance, which, for that matter, happens to have the same unit as an HTC. The main difference is that the inner-wall temperature instead of the fluid temperature acts as the sink temperature. The idea was then to use two distinct convective terms with two different sink temperatures.

III.A.2. Semi-heterogeneous Multiscale Coupling

To determine the expression of the gap conductance between the graphite sleeve and blocks, it is useful to go back to the original expression of radiative net rate between two infinitely long concentric cylinders [41], as given by:

$$q = \frac{A_1 \sigma (T_1^4 - T_2^4)}{\frac{1}{\varepsilon_1} + (A_1/A_2)(\frac{1}{\varepsilon_2} - 1)}, \tag{7}$$

where the subscripts 1 and 2 designate quantities pertaining to the inner and outer cylinders, respectively; A is the surface area with emissivity ε and local surface temperature T; and $\sigma \approx 5.67 \times 10^{-8}$ W/m^2/K^4 is the Stefan–Boltzmann constant. The heat flux (in W/m^2) through the gap via conduction and radiation is computed in BISON by using the assumption that $(A_2 - A_1)/A_2 \ll 1$, thus yielding:

$$q'' = \Bigg(\underbrace{\frac{k_g}{r \ln \frac{r_2}{r_1}}}_{\text{conduction}} + \underbrace{\frac{\sigma (T_1^2 + T_2^2)(T_1 + T_2)}{\frac{1}{\varepsilon_1} + \frac{1}{\varepsilon_2} - 1} \frac{r_1 + r_2}{2r}}_{\text{radiation}} \Bigg)(T_1 - T_2), \tag{8}$$

where r_1 and r_2 are the radii of the inner and outer cylinders, respectively—r being the radius where the heat flux is measured ($r = r_1$ and $r = r_2$ on the inner and outer cylinder, respectively)—and k_g is the gap thermal conductivity. In practice, because the macroscale mesh is not as axially refined as the pin-scale one, we decided to transfer quantities averaged over each of the five axial layers containing fuel (see Fig. 1(b)). Our first idea was to define an equivalent gap conductance $\overline{h}_{\text{gap},i}$ in each layer i in order to satisfy the following energy conservation equation:

$$Q_i = 2\pi r_2 H_{\text{block}} \left(\overline{h}_{\text{gap},i} (\overline{T}_{1,i} - \overline{T}_{2,i}) + \overline{h}_{\text{fluid, outer, i},i} (\overline{T}_{\text{fluid},i} - \overline{T}_{2,i}) \right), \tag{9}$$

where Q_i is the heat flux going into the graphite block of layer i, with height H_{block}; T_{fluid} is the local coolant temperature; $h_{\text{fluid, outer}}$ is the outer-wall HTC; and $\overline{X}_i$ corresponds to the average of any quantity X over layer i. However, this approach led to numerical instabilities. Instead, we defined an approximate gap conductance, mimicking in an average sense the one expressed in

Eq. 8:

$$\overline{h}_{\text{gap},i} \equiv \left(\frac{\overline{k}_{g,i}}{r_1 \ln \dfrac{r_2}{r_1}} + \frac{\sigma(\overline{T}_{1,i}^2 + \overline{T}_{2,i}^2)(\overline{T}_{1,i} + \overline{T}_{2,i})}{\dfrac{1}{\varepsilon_1} + \dfrac{1}{\varepsilon_2} - 1} \frac{r_1 + r_2}{2r_1} \right) . \tag{10}$$

This conductance was transferred to the macroscale model, along with the axially averaged inner-wall temperatures $\overline{T}_{1,i}$. The heat transfer due to convection, conduction, and radiation was then applied on the outer boundary of the (unmeshed) fuel cooling channels of the macroscale mesh (see Fig. 8), as per the following Robin BC:

$$q'' = \underbrace{\overline{h}_{\text{gap},i} \left(T - \overline{T}_{1,i}\right)}_{\text{conduction + radiation}} + \underbrace{\overline{h}_{\text{fluid, outer},i} \left(T - \overline{T}_{\text{fluid},i}\right)}_{\text{convection}}, \tag{11}$$

where T is the local solid temperature of the macroscale model. The same BC, but with the first term omitted, was applied to the CR cooling channels as well as to the fuel cooling channels inside the upper and lower replaceable reflector (layers 1, 2, 8, and 9 in Fig. 1(b)).

III.A.3. Homogeneous Multiscale Coupling

For the homogeneous macroscale model, we kept the same approach, the only difference being the homogenization of the surface source into a volumetric source. More specifically, the homogenized, layer-averaged gap conductance (in W/K/m^3) was defined as:

$$\widetilde{h}_{\text{gap},i} = \left(\frac{\overline{k}_{g,i}}{r_1 \ln \dfrac{r_2}{r_1}} + \frac{\sigma(\overline{T}_{1,i}^2 + \overline{T}_{2,i}^2)(\overline{T}_{1,i} + \overline{T}_{2,i})}{\dfrac{1}{\varepsilon_1} + \dfrac{1}{\varepsilon_2} - 1} \frac{r_1 + r_2}{2r_1} \right) \frac{2\pi r_2 n_{\text{rods}}}{S_{\text{block}}}, \tag{12}$$

where n_{rods} is the number of fuel rods in the (homogenized) graphite block with cross-sectional area S_{block}. The following volumetric source was then applied to the fuel columns (excluding the replaceable reflector layers), in addition to the convective volumetric source given by Eq. 5:

$$q''' = \widetilde{h}_{\text{gap},i} \left(T - \overline{T}_{1,i}\right), \tag{13}$$

where T is the local solid temperature of the macroscale model.

III.A.4. Assessment

To assess the benefits of our proposed coupling strategy, we would ideally quantitatively compare both the computational costs and differences in the solution (particularly the temperature fields). Nevertheless, to rigorously do so is made complicated by the fact that the old coupling approach is extremely slow for pseudo-transients, and thus very difficult to fully converge. More specifically, determining the optimal time step (i.e., for the old coupling, the largest possible time steps that preserve stability of the scheme) would be time consuming, making a perfectly fair comparison challenging. Therefore, the scope of this section is limited to giving the orders of magnitude of the computational gain, and not to precisely determine the achieved level of speed-up. We also emphasize that the new, convective-based coupling does not seem to suffer from numerical instability during the pseudo-transient—independent of time step size—whereas the heat-flux-based coupling entails drastic stability requirements.

Because the computational cost of the old coupling is so large, comparisons were only performed using the homogeneous multiscale coupling presented in Section III.A.3. The only difference between both models are the coupling terms and, for the pseudo-transient, the time-stepping strategies and final end times. The end time for the new coupling, chosen to be 5×10^6 s, is too long for the heat-flux-based coupling, as the maximum time step appears to be on the order of 50–100 s. Thus, we limited it to 5×10^4 s, with the understanding that the solution has not yet reached a thermal equilibrium. Despite that, the computational cost, summarized in Table IV, shows a runtime improvement of more than 65x. Reaching a true thermal equilibrium would thus require several orders of magnitude more computational effort for the heat flux approach.

TABLE IV
Runtime (for one Sawtooth node [48 processors]), of the homogeneous models, using heat-flux- vs. conductance-based coupling.

Model	Pseudo-transient end time (s)	Steady-state runtime (hrs)
Heat flux based	5×10^4	48
Conductance based	5×10^6	0.73

III.B. Effective Radial Thermal Conductivity

For the homogeneous macroscale model to accurately represent the heat transfer through the graphite blocks, we must account for the additional thermal resistance induced by the fuel and CR cooling channel holes. Therefore, we desire to derive an anisotropic effective thermal conductivity—which is to only be reduced in the radial direction—that accounts for these holes. Common techniques include considering the various constituents as either serial or parallel thermal resistors [3] in order to compute the effective thermal conductivity of porous media considered as a whole. However, we only desired to compute how the holes in the graphite blocks affect the thermal conductivity. We therefore excluded this approach and instead considered two separate alternatives: (1) a global approach directly leveraging a semi-heterogeneous mesh to explicitly model these holes, and (2) one relying on Maxwell's theory, as was the case in [42]. We then assessed both approaches by comparing them to directly using the semi-heterogeneous macroscale model.

III.B.1. Approach

Because we were mostly interested in the radial effect inside the core, we restricted the mesh shown in Fig. 8 to a 2-D configuration, and removed the RPV (in purple in that same figure). Although the mesh does not currently include the inter-column gaps—which would further increase the thermal resistance—the methodology we propose could still be applied were they to be added.

A typical method of determining the effective thermal conductivity is to impose temperatures across a domain and then measure the heat flux flowing through it. In our case, this could be done by imposing the temperatures at the center of the core and at the radial outer boundary of the PR. Nevertheless, the resulting thermal conductivity accounts for the thermal resistance when radially crossing the entire core, whereas the heat crossing the fuel cooling channels in the last ring of fueled assemblies must skirt comparatively very few holes to reach the outer boundary of the mesh. Therefore, this approach yields unsatisfactory results and significantly underestimates the effective thermal conductivity.

Rather, we imposed both a uniform heat flux coming out of the fuel cooling channels as well as the temperature on the outer boundary via a pseudo-Dirichlet BC in order to exactly preserve the global energy balance [38], and determined the effective thermal conductivity by

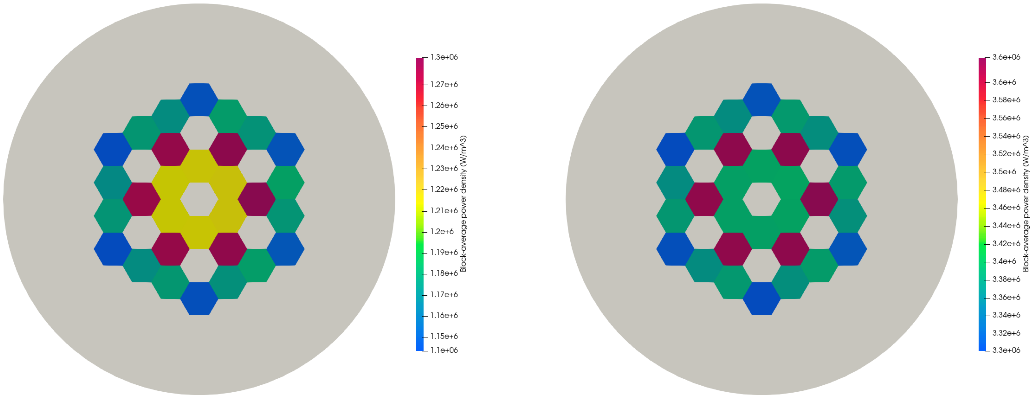

(a) 9 MW.

(b) 30 MW.

Fig. 9. Steady-state block-averaged fission power density (in W/m^3) for the center fuel layer.

using the measured temperature gradient. The justification for applying a uniform heat flux lies in the relatively flat power density radial distribution shown in Fig. 9—which also corresponds to the assumed decay heat radial distribution. The flatness of the power density radial distribution is due to the higher fuel enrichment of the outer fuel columns (see Fig. 1). Fig. 10 shows the temperature profile obtained by imposing a total heat flux of 250 kW and a radial outer boundary temperature of 400 K.

We approximated the theoretical total heat flux leaving the outer boundary of the domain, $\partial\mathcal{D}$, as:

$$\mathcal{Q} = \int_{\partial\mathcal{D}} -k\vec{\nabla}T \cdot \vec{n}\mathrm{d}x \approx -2\pi R_1 H k_{\mathrm{eff}} \frac{T_1 - T_0}{R_1 - R_0}, \tag{14}$$

where k_{eff} is the effective thermal conductivity, $H = 2.9$ m is the height of the active core, R_1 is the PR outer radius, T_1 is its imposed temperature, T_0 is the average temperature of the blocks containing fuel rods, and R_0 is the effective inner radius, defined as:

$$R_0 \equiv \frac{1}{N_f} \sum_{i=1}^{N_f} \sqrt{x_i^2 + y_i^2} \approx 0.794 \text{ m}, \tag{15}$$

where N_f is the total number of fuel columns and (x_i, y_i) are the coordinates, in the radial plane, of

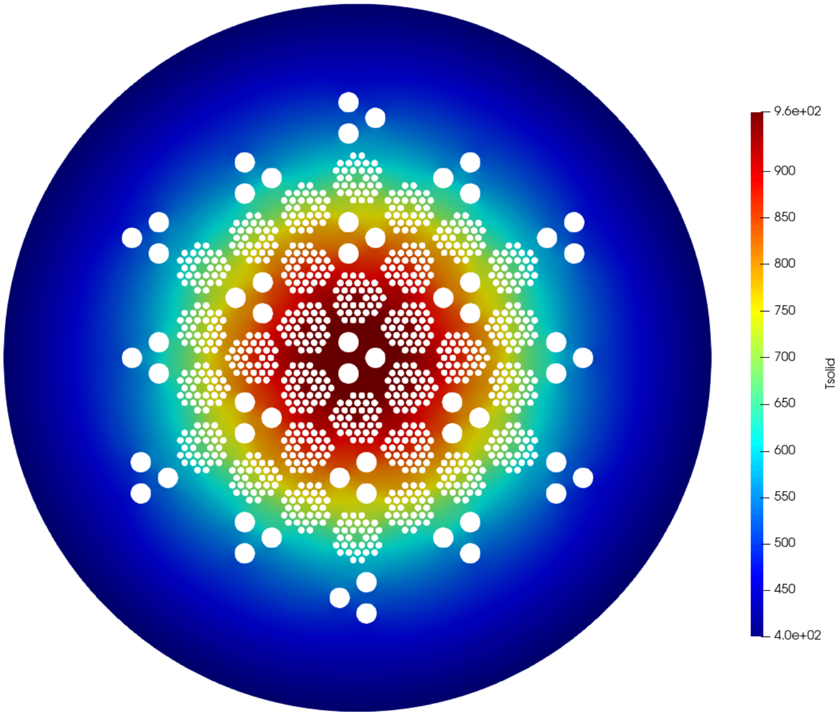

Fig. 10. Temperature profile obtained by imposing $\mathcal{Q} = 250$ kW and a radial outer boundary temperature of 400 K.

the center of the column of index i. We then can express the effective radial thermal conductivity as:

$$k_{\text{eff}}(\mathcal{Q}, T_1) \equiv \frac{\mathcal{Q}}{2\pi R_1 H} \frac{(R_1 - R_0)}{T_0 - T_1}. \tag{16}$$

This quantity obviously depends on $\mathcal{Q}$ and T_1 (since they are the BCs of the problem) and could have a complicated dependency, given that the thermal conductivity of the graphite blocks depends on local temperature. Specifically, the (unmodified) thermal conductivity of IG-110 graphite is obtained by using a weighted average of the expressions at 0 and 660 EFPDs in [3], thereby yielding, at 373 EFPDs:

$$k(T) = 66.32 - 4.994 \times 10^{-2}\, T + 1.712 \times 10^{-5}\, T^2, \tag{17}$$

where k is in W/(K-m) and T is the local graphite temperature in K, for T between 300 and 1400 K. To preserve this dependency with respect to the local temperature, and to directly obtain a sense of how much the thermal conductivity is reduced radially, we define the following factor:

$$\alpha(\mathcal{Q}, T_1) \equiv \frac{k_{\text{eff}}}{\overline{k}}, \tag{18}$$

where $\overline{k}$ is the average thermal conductivity over the graphite blocks and PR. We then define the *global* anisotropic effective thermal conductivity of the homogeneous macroscale model as:

$$\vec{\vec{k}}_{\text{eff}}(T) \equiv \begin{bmatrix} \alpha & 0 & 0 \\ 0 & \alpha & 0 \\ 0 & 0 & 1 \end{bmatrix} k(T), \tag{19}$$

with α applied in the radial directions and an unchanged thermal conductivity in the axial direction. We determined the value of α from Fig. 11, which evaluates it under steady-state conditions for various values of $\mathcal{Q}$ and T_1. It did not vary significantly for the typical values of $\mathcal{Q}$ and T_1 that we encountered during the LOFC simulations. Indeed, if we consider that $\mathcal{Q}$ will be on the order of the average total decay heat during the first 5–10 hours of the transient, it would be around 100 and 250 kW for the 9 and 30 MW cases, respectively. This derivation was performed on a

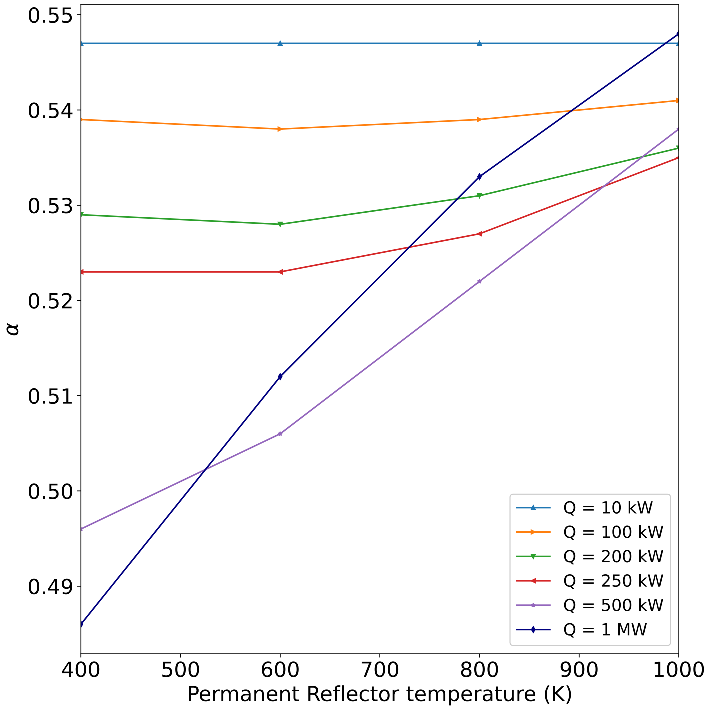

Fig. 11. Values of α as a function of $\mathcal{Q}$ and the permanent reflector temperature, T_1, using Eq. 18.

2-D case, using a linear heat flux averaged over the height of the active fuel. However, in the 3-D case, because heat can also be dissipated through the axial reflectors—which account for 4/9ths of the total height—the average linear heat flux is expected to be smaller. Therefore, for the sake of simplicity, we chose a constant value for α of 0.54 for all cases. We refer to the resulting $\vec{\vec{k}}_{\text{eff}}$ as the global effective homogeneous thermal conductivity.

Another approach is to utilize the analytical expression obtained for α by using Maxwell's theory, as presented in [42]. If we consider empty cylinders with zero thermal conductivity in Eq. 6.2.14 of [42], we obtain:

$$\alpha_{\text{AMEC}} = \frac{s}{2-s}, \tag{20}$$

where s is the surface fraction of the graphite blocks occupied by graphite (with $1-s$ being the fraction occupied by the holes). In particular:

$$\alpha_{\text{AMEC}} = \begin{cases} 0.4407 & , \quad \text{for 33-pin fuel blocks,} \\ 0.4656 & , \quad \text{for 31-pin fuel blocks,} \\ 0.5179 & , \quad \text{for CR blocks,} \\ 1 & , \quad \text{for PR blocks.} \end{cases} \tag{21}$$

We emphasize that this approach, which we call the AMEC approach, is also an approximation, since the derivation assumes an infinite lattice of cylinders embedded in a matrix, with all the materials having a fixed thermal conductivity—whereas we are mixing several types of assemblies with finite dimensions and considering a temperature-dependent graphite thermal conductivity. On the other hand, our global approach accounts for both these effects but applies a uniform value for α (independently of the blocks).

III.B.2. Assessment of the Homogenized Solution

To assess—via both the global and AMEC approaches (i.e., using $\alpha = 0.54$ and $\alpha = \alpha_{\text{AMEC}}$ in Eq. 19, respectively)—the accuracy of the anisotropic effective thermal conductivity by using a homogeneous macroscale model, we compared the corresponding LOFC results to the semi-heterogeneous calculation. Were the effective thermal conductivity perfect, the results should match exactly. Thus, in this study, the latter can be considered as the reference solution.

Fig. 12 focuses on the 9 MW results. The short- and long-term evolutions of the fission power are shown in Fig. 12(a) and Fig. 12(b), respectively, and the corresponding average fuel temperatures are shown in Fig. 12(c) and Fig. 12(d), respectively. Within the first few minutes, the fission power decrease is very similar because it is primarily driven by fuel temperature feedback. After 15 minutes or so, the differences become apparent, with the semi-heterogeneous fission power dropping at a near-constant rate until it saturates below 10 W (due to the neutron sources), whereas the homogeneous solutions slow down—partly because the fuel temperature is lower than for the reference case—before reaching the same power levels, with the global effective thermal conductivity being a little closer to the reference solution. This better agreement is even more evident at later times, with the re-criticality time and subsequent power peak being extremely close, whereas the AMEC re-criticality time is about an hour early.

The 30 MW comparison is shown in Fig. 13. The main difference is that the overall heat flux added to the graphite blocks is larger and the axial gradient a lot more significant. This time, both effective thermal conductivities perform quite well at early times, with the fission power evolving very similarly to that in the semi-heterogeneous case (see Fig. 13(a)). The average fuel temperature is also quite close during the first half hour (see Fig. 13(c)), but starts to noticeably differ over the course of several hours (see Fig. 13(d)). The re-criticality time is fairly well reproduced, but for the global approach is still about an hour late. For the AMEC approach, it is about an hour early (see Fig. 13(b)). However, the peak power better matches the reference value in the former case.

Overall, we obtained reasonable results for the effective thermal conductivities by using both the global approach presented herein as well as the AMEC formula. However, we did not quite reproduce the fine behavior of the solution, particularly in terms of temperature feedback. The main advantage of the homogeneous approach is the significant decrease in runtime—by a factor of about 5–8 in terms of CPU hours, as summarized in Table V—thus potentially maintaining the appeal of this approach, particularly for computationally demanding applications such as uncertainty quantification and sensitivity analysis.

TABLE V
Runtime with homogeneous and semi-heterogeneous macroscale models and speed-up in terms of CPU hours.

Model	Processors (CPU)	Steady-state runtime (hrs)	Speed-up	Transient runtime (hrs)	Speed-up
Homogeneous	48	0.73	8.2	17.4	5.3
Semi-heterogeneous	196	1.5		23.0	

III.C. Study of Early Behavior

III.C.1. Motivation

The motivation behind this preliminary study was to understand what drives the decrease in fission power within the first half hour of the transient. Following a LOFC event, the sudden loss of heat removal creates a sharp reactivity decrease due to negative temperature reactivity coefficients, and the reactor remains sub-critical for many hours. Nevertheless, some numerical models have exhibited an early behavior inconsistent with the fission power measured data, as

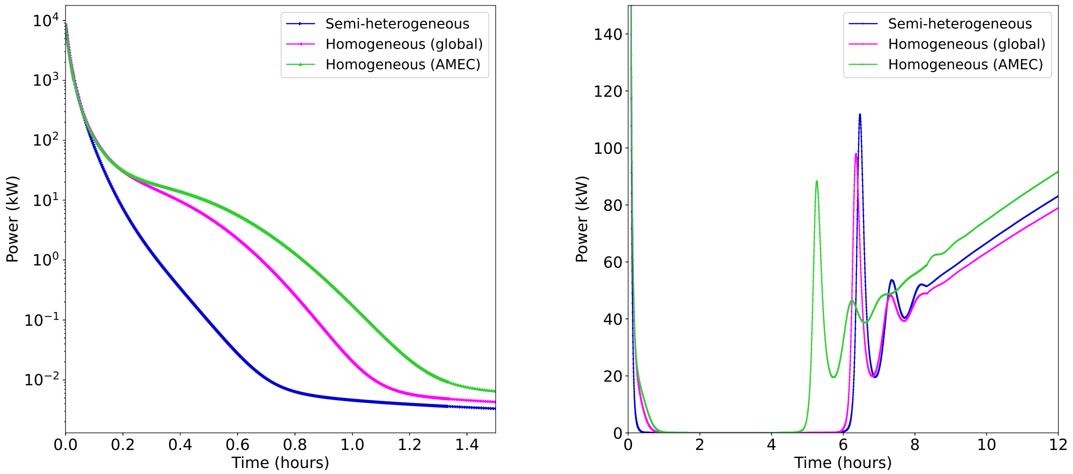

(a) Power (first 1.5 hours).

(b) Power (first 12 hours)

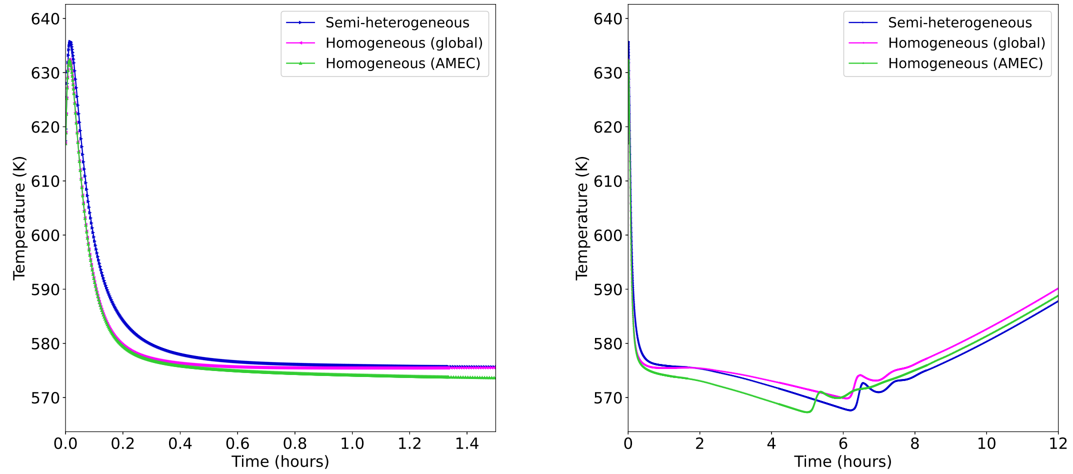

(c) Average fuel temperature (first 1.5 hours).

(d) Average fuel temperature (first 18 hours).

Fig. 12. Power and temperature evolution of the semi-heterogeneous approach, as compared to those of the homogeneous approach using the global and AMEC anistropic effective thermal conductivities for the 9 MW case.

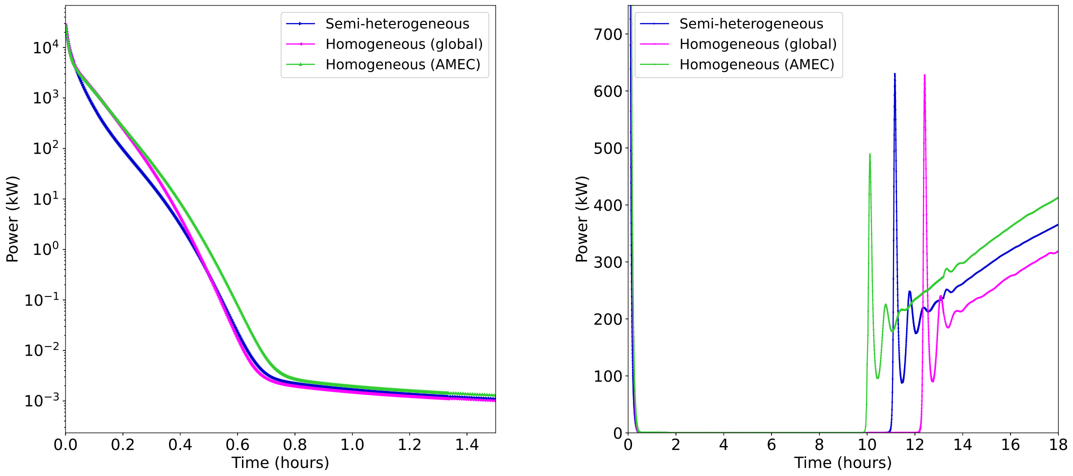

(a) Power (first 1.5 hours).

(b) Power (first 18 hours)

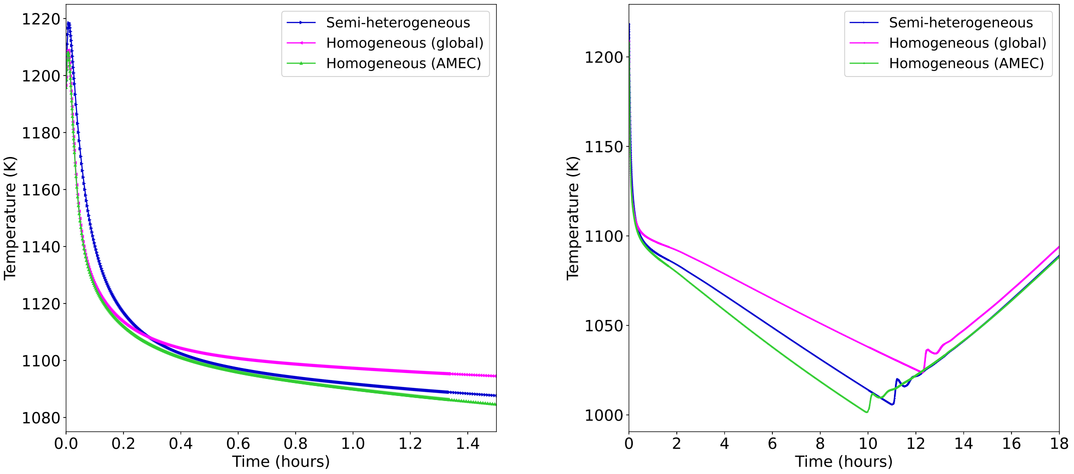

(c) Average fuel temperature (first 1.5 hours).

(d) Average fuel temperature (first 18 hours).

Fig. 13. Power and temperature evolution of the semi-heterogeneous approach, as compared to the homogeneous approach using the global and AMEC anistropic effective thermal conductivities for the 30 MW case.

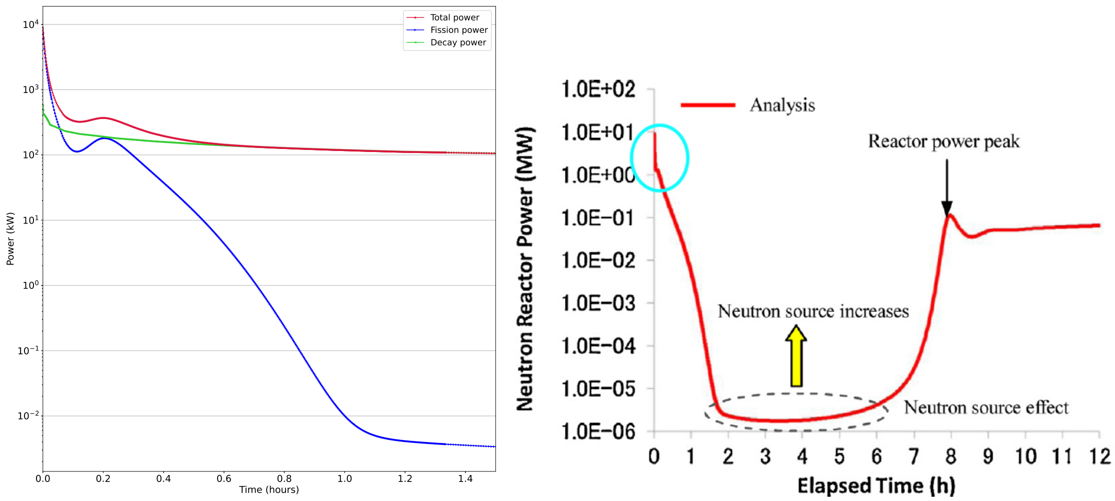

(a) Results generated using the model described in [14].

(b) (Figure courtesy of [2].) A cyan circle has been added to the figure to visualize the possible early re-criticality.

Fig. 14. Examples of HTTR LOFC numerical models displaying an early re-criticality (or at least an early reactivity increase leading to a sharp curbing of the fission power decrease).

shown in Fig. 14. In particular, Fig. 14(a) shows the results obtained with a model derived from [14], and compares the predicted fission power (in blue) to the measured one (in orange), featuring an early re-criticality—exhibited by a small rise in power in the first 10 minutes of the transient—that does not appear in the experimental data (see Figure 6 in [2]). Similarly, Fig. 14(b), despite being insufficiently zoomed-in to conclude categorically whether an early re-criticality is obtained, also displays a short stagnation of the fission power at around 1 MW, before the power resumes its decrease and drops to a few Watts. Though we are unaware of any peer-reviewed work focusing on this early stage of the transient, we believe it to be a very valuable area of research, since comparison against experiments can provide a wealth of information in terms of temperature feedback coefficients and overall rod-wise heat transfer—for which limited validation data exist (at least regarding HTTR).

Although the experimental data do not exhibit any re-criticality or even significant slowing in the reduction of fission power (see Fig. 14(a)), this does not mean that such a phenomenon is inherently unphysical. In fact, such behavior has been observed in other models featuring gas gaps between the fuel and core heat transfer media [43].

III.C.2. Single-Rod Model

To understand which parameters affect the early behavior of the decrease in fission power, we considered a simplified single-rod model (see Section II.D) coupled only to a point kinetics (PKE) model, under prototypical 9 MW conditions, with the following specifications:

- A total power of 1.9 kW—corresponding to the average power per rod in the core with a total power of 9 MW—is uniformly deposited in the fuel compact.
- Of that power, 2.5% is assumed to come from decay heat. This is roughly the average decay heat contribution over the first 15 minutes after shutdown.
- Radial losses are deactivated to study the rapid thermal response of the fuel rod (over the first 15 minutes or so).
- At the initial time, any heat loss via convection is removed so as to simulate a LOFC, thereby making the rod thermally insulated.
- The PKE parameters, as described in Table VI and estimated by Griffin with the semi-heterogeneous multiscale and multiphysics model presented in Section III.A.2, are assumed.
- The fuel and moderator reactivity coefficients are input parameters.
- Xenon decay is neglected, as its impact generally only becomes significant over the course of several hours.

TABLE VI
PKE parameters used in the single-rod model. λ_i and β_i are the decay constants and delayed neutron fractions, respectively. Λ is the mean generation time.

Delayed Group	λ_i (s^{-1})	β_i (pcm)	Λ (s)
1	1.3338×10^{-2}	23.4	9.384×10^{-4}
2	3.2724×10^{-2}	120.7	
3	1.2081×10^{-1}	115.7	
4	3.0315×10^{-1}	259.9	
5	8.5107×10^{-1}	107.8	
6	2.8583×10^{0}	45.1	
Sum		672.6	

In terms of reactivity coefficients, we selected the values based on Table II and the typical 9 MW steady-state temperature fields—namely, $\alpha_f \approx -6$ and $\alpha_m \approx -5.7$ pcm/K for the fuel and moderator feedback coefficients, respectively. We also perturbed them to assess what generally causes re-criticality.

Fig. 15 shows the fission power, fuel/moderator temperatures, and total reactivity as a function of time for four combinations of (α_f, α_m). In all cases, the fuel temperature rapidly increases until the heat source decreases to levels lower than what is transferred to the graphite sleeve and block. At that point, the fuel temperature starts dropping, eventually reaching levels lower than the initial temperature, thereby adding positive reactivity. In the meantime, the graphite temperature also increases, thus also adding negative reactivity. The combined effect is what determines whether re-criticality can occur. It is therefore no surprise that the total reactivity reaches larger values when α_f is larger (in magnitude) and α_m is smaller (in magnitude). For the nominal conditions ($\alpha_f = -6$ and $\alpha_m = -5.7$ pcm/K), the reactivity curve peaks at around -115 pcm at about 500 s. If α_f is doubled or α_m halved, the power decrease slows down after around 200 s—close to the time at which the fuel temperature falls below its initial value—and the total reactivity exceeds -50 pcm. If both effects are combined ($\alpha_f = -12$ and $\alpha_m = -2.9$ pcm/K), the fission power plateaus for more than a minute before decreasing again, and almost reaches re-criticality (total reactivity exceeding -13 pcm after 6 minutes).

To achieve close agreement with the experimental fission power evolution, the quantity $\alpha_f \Delta T_f + \alpha_m \Delta T_m$, where $\Delta T = T(t) - T(0)$, must be closely reproduced. Therefore, if either reactivity coefficients α_f or α_m are wrong, and/or if the heat transfer is not properly predicted (i.e., ΔT_f and ΔT_m), whether by the PKE or the Griffin model, the power will decrease at a different rate (assuming the kinetics parameters were accurately captured). Since the experimental data do not include in-core temperatures and JAEA has not yet provided the measured reactivity coefficients, this early behavior represents an alternate way of validating these quantities in an integrated sense.

IV. LOFC SIMULATION RESULTS

This section details our most accurate results to date, achieved using the semi-heterogeneous macroscale model and the new coupling method presented in Section III.A.

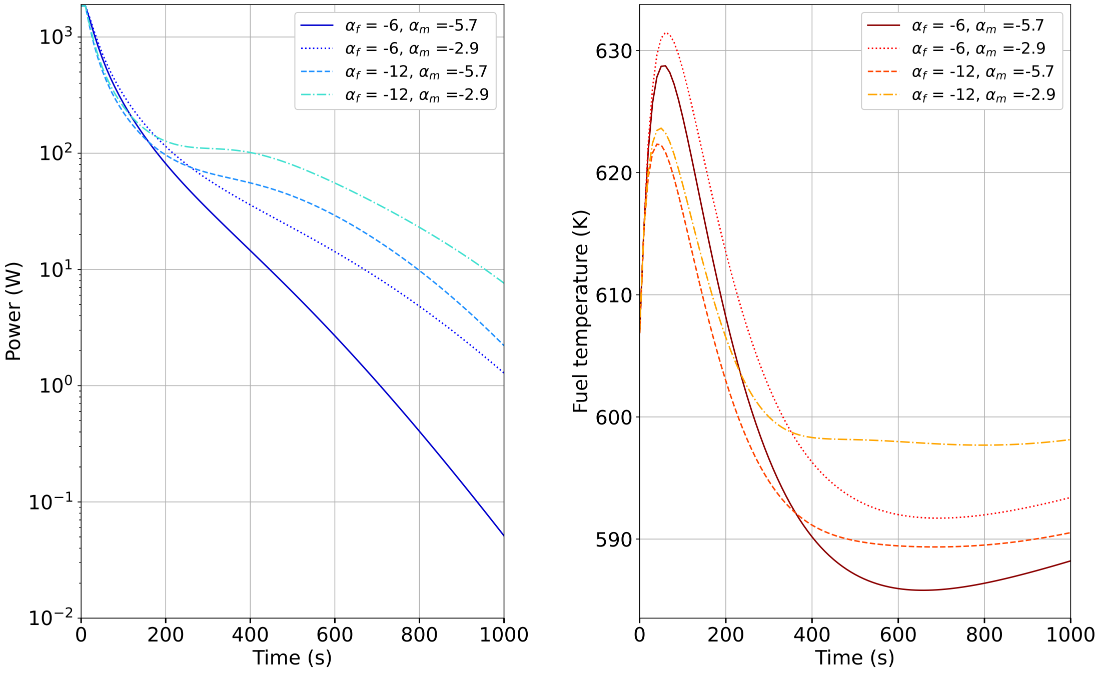

(a) Power

(b) Fuel temperature

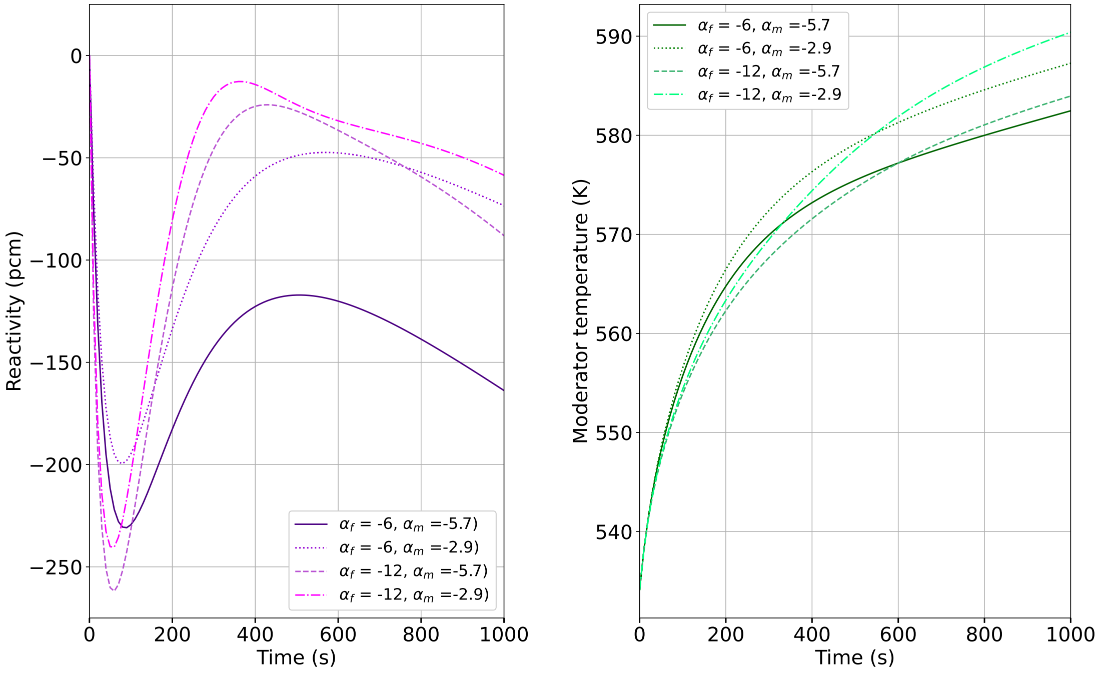

(c) Reactivity

(d) Moderator temperature

Fig. 15. Early behavior of a single fuel rod, following a loss of convective cooling for different values of the fuel and moderator feedback coefficients (α_f and α_m, respectively, in pcm/K).

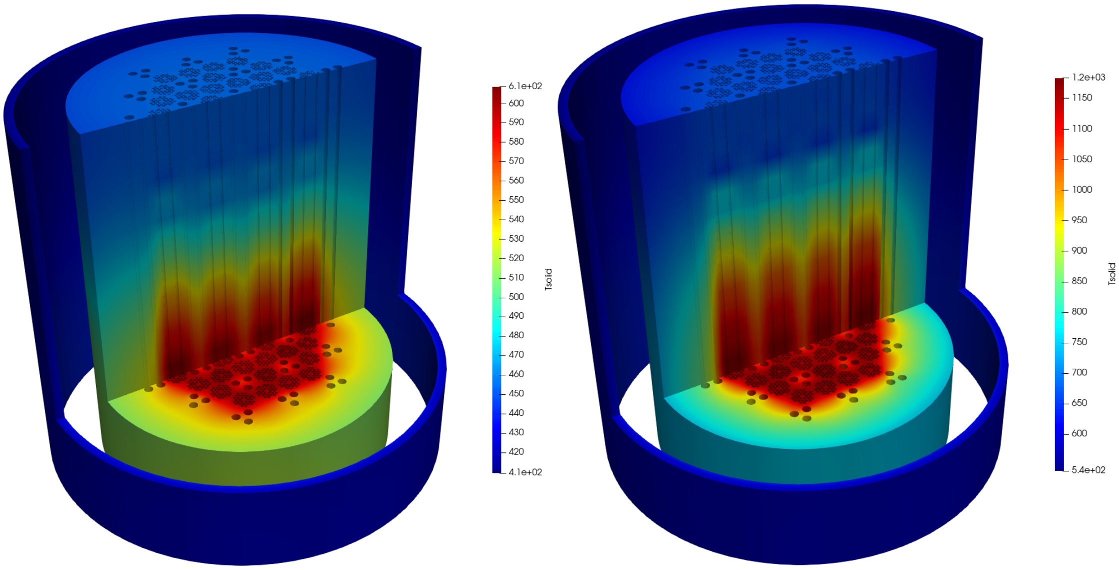

(a) 9 MW (b) 30 MW

Fig. 16. Steady-state graphite and RPV temperature distribution (in K).

IV.A. Steady-State Solutions

Fig. 16 shows the steady-state temperature distributions from the semi-heterogeneous full-core heat transfer model for the 9 and 30 MW transients. We also assess the steady-state numerical solution in terms of the initial multiplication factor.

In particular, the multiplication factors (see Table VII) should theoretically be very close to 1 at the beginning of the transient (and exactly 1 if no neutron sources were present). The 9 and 30 MW coupled steady states are about 1,260 and -370 pcm off. Given the large overall uncertainty (on the order of 700–1000 pcm [1]), which mostly stems from graphite impurities, this seems quite acceptable.

TABLE VII

Multiphysics steady-state multiplication factors in the semi-heterogeneous macroscale model.

Power (MW)	k_{eff}
9	1.01258
30	0.99629

IV.B. 9 MW LOFC Post-experiment Predictions

Next, we compare our model to the experiment for the 9 MW LOFC. Fig. 17 gives the evolution of the numerical fission and decay powers over time, and allows for comparing the former to the experimental data, whether for short or long durations. The fission power drops from the initial 8.43 MW to about 4 W (i.e., by more than six orders of magnitude) in about an hour, following the same trend seen in the experimental data, albeit with some anticipation, indicating an overall reactivity feedback that is too negative. After about an hour, the neutron flux stops decreasing and is mostly driven by spontaneous fission from the Cf-252 neutron sources, as the core remains in a subcritical configuration. Simple point kinetics theory predicts the steady-state flux (and power) in a subcritical configuration with external sources to be inversely proportional to $(1-k_{\text{eff}})$, where k_{eff} is the multiplication factor. It is therefore unsurprising to see the power slowly increase as the reactivity becomes less and less negative. During that phase, the residual decay heat is the only remaining significant heat source. As the core cools down and the Xe-135 decays, positive reactivity is slowly added to the core until re-criticality is reached. The current simulation predicts a re-criticality time of 4 hours and 43 minutes, and a subsequent power peak at 6 hours and 28 minutes after the initial accident, while the measurement indicates 6–7 hours [2] and around 8 hours, respectively. The experimental value for the first fission power peak after re-criticality is around 275 kW [3], whereas the predicted value is about 112 kW, with an additional 67 kW from decay heat. Underestimation of that power peak also suggests the temperature feedback to be too negative. At that point, power oscillates until the total power matches the power removed by the VCS. As such, the fission power continues to slowly increase to compensate for the long-term decrease in decay heat. Underestimation of the fission power over longer durations ($t > 10$ hours)—a value that should be around 150–200 kW after 12 hours [2]—suggests that the VCS model does not remove enough heat.

Fig. 18 displays the fuel and moderator average temperatures predicted throughout the transient. The average fuel temperature rapidly increases from 617 to 636 K in the first minute, which is the main reason why the fission power drops so sharply (at that point, by more than 70% of its initial value). The amount of heat deposited in the fuel compact is then too low to prevent the fuel temperature from eventually decreasing. Less than 3 minutes after the transient begins, it drops below its initial value and stabilizes at around 577 K after 20–30 minutes. Then

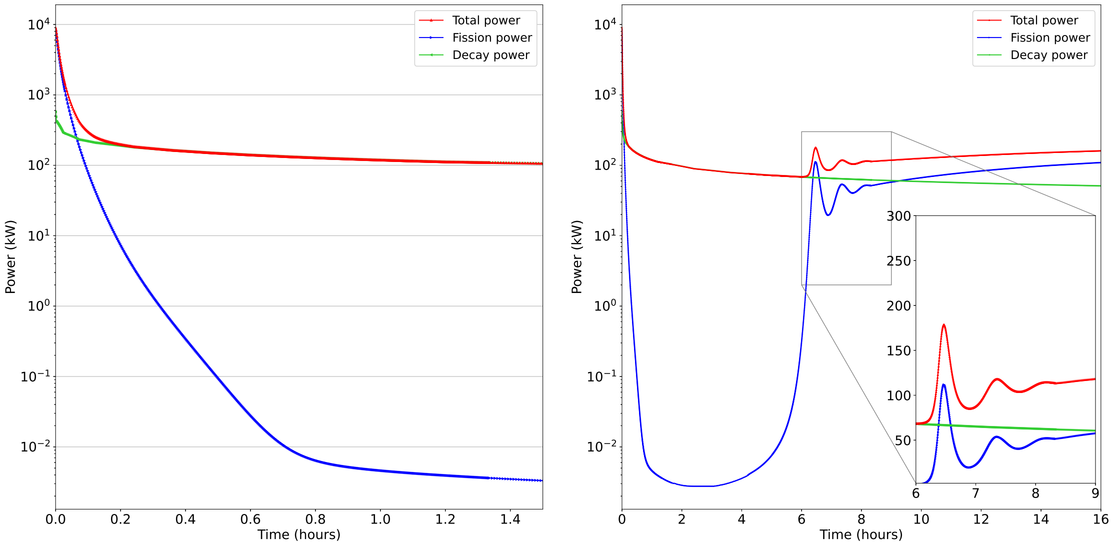

(a) First 1.5 hours.

(b) First 16 hours.

Fig. 17. Evolution of the heat sources (fission and decay power) for the 9 MW LOFC transient.

it remains mostly constant, reaching around 568 K when the fission power again rises shortly after re-criticality. In the meantime, the average graphite block temperature slowly increases from 522 to about 534 K, where it mostly plateaus until the fission power once again becomes significant. As the core approaches a new thermal equilibrium (for $t > 12$ hours) and the fission power rise is very slow (only to compensate the equally slow decrease in decay heat), the temperature of the core increases gradually, adding negative reactivity that counteracts the positive reactivity added by xenon decay.

Fig. 19 gives a better understanding of the total and xenon reactivity during the transient. Initially, the behavior of the core is driven by temperature effects, with both moderator and fuel average temperatures increasing, yielding a total reactivity of almost -215 pcm. As the fuel temperature decreases faster than the moderator heats up[b], the total reactivity starts increasing again after 1–2 minutes, and is driven back to negative values by the xenon buildup. After a few hours, the total reactivity curve remains above that of the xenon, indicating that from that point until much later on, the reactivity due to temperature is positive. This result is mostly consistent with the reactivity results of the JAEA numerical model, reproduced in Fig. 20. In fact, the average fuel and moderator temperatures that can be inferred by taking the opposite of the

---

[b] Note also that the moderator reactivity coefficient is not as negative as that of the fuel.

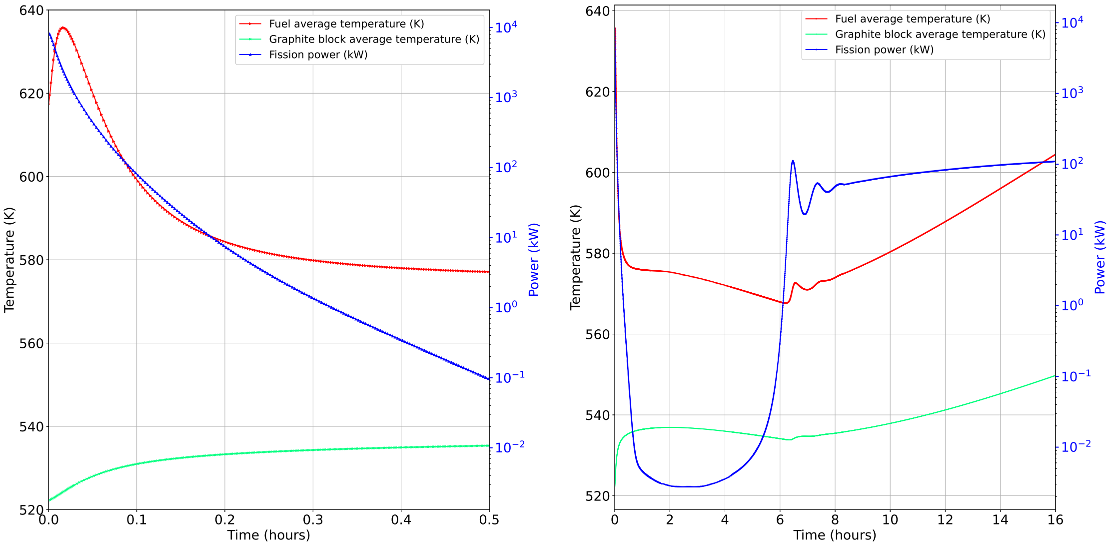

(a) First 1.5 hours.

(b) First 16 hours.

Fig. 18. Evolution of the average fuel and graphite block temperatures for the 9 MW LOFC transient.

temperature-driven reactivity curves in Fig. 20 show a behavior that, during the sub-critical phase of the transient, is very similar to the behavior seen in Fig. 18.

IV.C. 30 MW LOFC Pre-experiment Predictions

Finally, we present our current pre-experiment predictions for the 30 MW LOFC. The main difference between this test and the 9 MW LOFC case is that the core is initially operated at 30 MW, leading to a much larger axial temperature gradient: namely, on the order of 110 K/m for the radially averaged fluid and moderator temperatures, as compared to about 30 K/m for the 9 MW steady-state configuration. The other difference is that no experimental data are currently available, as the test is planned to be performed in the near future.

Fig. 21 gives the evolution of the numerical fission and decay powers over time. The fission power drops from the initial 28 MW to just a few W (i.e., by almost eight orders of magnitude) in the first 40 minutes, then stabilizes at around 0.5 W. The reason it reaches a lower value than for the 9 MW case is that the neutron sources are assumed to be older (6 vs. 4 years old), as shown in Table III. The current simulation predicts a re-criticality time of 9 hours and 35 minutes, and a subsequent power peak at 11 hours and 10 minutes after the initial accident. The fission power

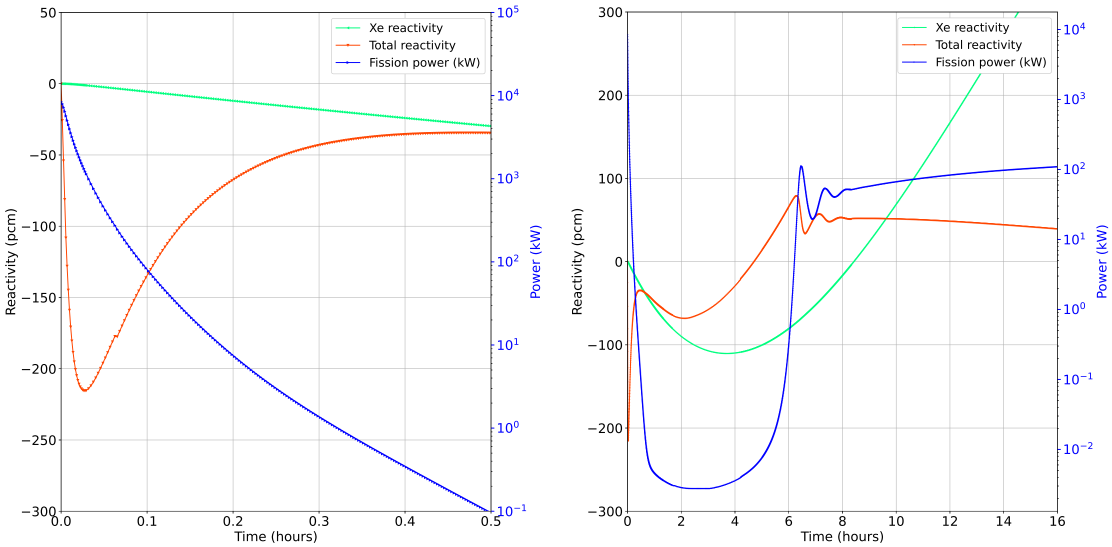

(a) First 1.5 hours.

(b) First 16 hours.

Fig. 19. Evolution of the xenon and total reactivity for the 9 MW LOFC transient.

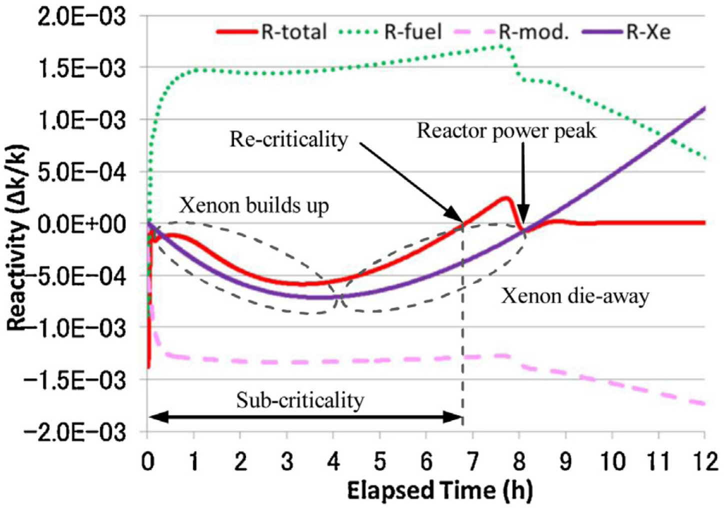

Fig. 20. 9 MW LOFC reactivity evolution predicted by the JAEA numerical model. (Picture courtesy of [2].)

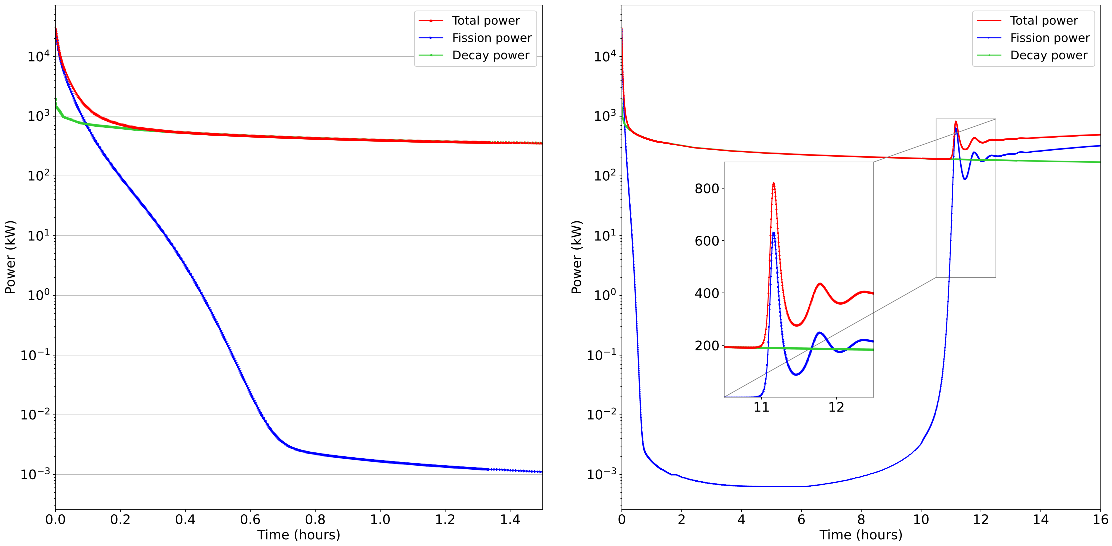

(a) First 1.5 hours.

(b) First 16 hours.

Fig. 21. Evolution of the heat sources (fission and decay power) for the 30 MW LOFC transient, along with the measured fission power.

peak after re-criticality is projected to be about 630 kW, with an additional 183 kW from decay heat.

Fig. 22 displays the fuel and moderator average temperatures measured throughout the transient. The average fuel temperature increased from 1198 to 1218 K in the first 30 seconds, rapidly lowering the fission power (at that point, by about 50% of its initial value). The amount of heat deposited in the fuel compact was then too low to prevent the fuel temperature from eventually decreasing. About 100 s after the beginning of the transient, the temperature returned to its initial value, briefly plateauing at around 1096 K, when the power drop was slightly slower. It then resumed its decrease, this time almost linearly until reaching re-criticality, at which point the average fuel temperature had almost reached 1006 K. In the meantime, the average graphite block temperature increased from 910 K to a maximum of about 947 K at around 1 hour, before decreasing to about 900 K. After re-criticality, both the fuel and moderator temperatures gradually increased to compensate for the positive reactivity added by xenon decay.

Fig. 23 shows the evolution of the total and xenon reactivity during the transient. As in the 9 MW case, the total reactivity rapidly increases after reaching a local minimum of -183 pcm within the first minute; it then reaches around -100 pcm before dropping again, driven by the

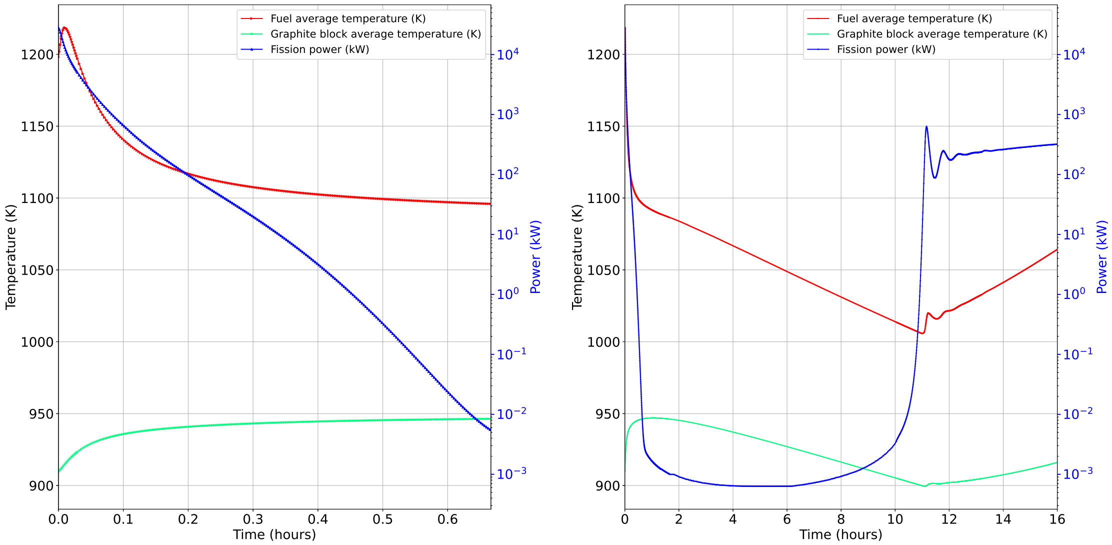

(a) First 1.5 hours.

(b) First 16 hours.

Fig. 22. Evolution of the average fuel and graphite block temperatures for the 30 MW LOFC transient.

xenon reactivity. Nevertheless, the xenon peak is a lot more pronounced, with a minimum induced reactivity of -630 pcm, as compared to -110 pcm for the 9 MW case.

Overall, the predicted transient behavior is very comparable to that of the 9 MW case, with a significantly later re-criticality time and a larger power peak. This difference is mostly driven by the much larger xenon peak, but also by the slower cooling of the core, with the reactivity due to the fuel and moderator temperatures not becoming significantly positive until almost 5 hours into the transient (as compared to less than 1 hour for the 9 MW simulation). The experimental data for the upcoming test will be of great interest in further assessing this transient prediction.

V. CONCLUSION

In summary, we have presented several improvements to a multiphysics, multiscale model simulating past and future HTTR LOFC experiments, using a 3-D full-core SPH-corrected Griffin input for neutronics, macroscale and pin-level heat transfer BISON models and thermal-hydraulics RELAP-7 channels. We proposed a new approach for coupling the macroscale and pin-scale models, relying on the HTC and gap conductance to drastically speed up the numerical convergence in comparison to using heat fluxes. While the latter imposes drastic stability conditions on the

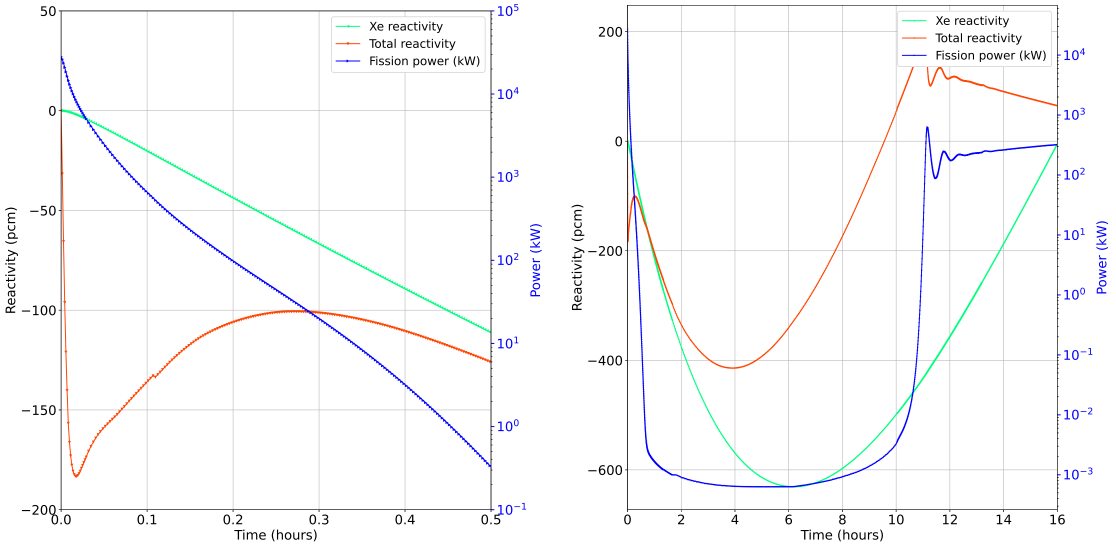

(a) First 1.5 hours.

(b) First 16 hours.

Fig. 23. Evolution of the xenon and total reactivity for the 30 MW LOFC transient.

time step size, the former does not seem to suffer from any restriction other than time discretization error, thus yielding the steady-state solution about two orders of magnitude faster. We then derived a radial effective thermal conductivity for use with a homogeneous macroscale model and compared it to a semi-heterogeneous model, with all the holes being explicitly represented, ultimately producing similar results in terms of general behavior—for a fraction of the computational cost. Given the persisting differences in the temperature feedback, this approach can be seen as a lower order approximation that could be attractive for repeated calculations such as those needed for uncertainty qualification and sensitivity analyses. Next, we studied the early behavior of the reactor following a LOFC event in order to further leverage fission power measurements to validate numerical models, and showed the importance of reactivity feedback at early times. Lastly, we presented our latest numerical simulations for the post- and pre-experiment (9 and 30 MW, respectively) LOFC experiments, but are fully aware that the uncertainty in the results remains large, partly because the in-core validation data are mostly limited to fission power measurements, and also because reactivity coefficients are currently unavailable.

Before further improving the numerical model, it will be important to quantify the uncertainty in our results. In the near term, we plan to conduct an uncertainty quantification and sensitivity analysis preliminary study to assess the impact of various parameters on the main quantities of interest in this transient—namely, early behavior (including maximum fuel temperature), re-criticality time, and the subsequent power peak.

ACKNOWLEDGMENTS

This manuscript was authored by Battelle Energy Alliance, LLC under contract no. DE-AC07-05ID14517 with the U.S. Department of Energy. The U.S. Government retains and the publisher, by accepting the article for publication, acknowledges that the U.S. Government retains a nonexclusive, paid-up, irrevocable, worldwide license to publish or reproduce the published form of this manuscript, or allow others to do so, for U.S. Government purposes.

This research was funded by the U.S. Department of Energy Advanced Reactor Technologies Program for Gas Cooled Reactors (ART-GCR). It made use of the resources of the High Performance Computing Center at Idaho National Laboratory, which is supported by the Office of Nuclear Energy of the U.S. Department of Energy and the Nuclear Science User Facilities under contract no. DE-AC07-05ID14517.

The authors would like to recognize John Shaver for his excellent and prompt technical review of this manuscript.

Disclaimer: This work is not part of the NEA Loss of Forced Coolant (LOFC) Project, and was performed by INL leveraging information available in the open source domain.

REFERENCES

[1] J. D. Bess and N. Fujimoto, "Benchmark Evaluation of Start-Up and Zero-Power Measurements at the High-Temperature Engineering Test Reactor," *Nuclear Science and Engineering*, **178:3**, 414 (2014); 10.13182/NSE14-14.

[2] K. Takamatsu, X. L. Yan, S. Nakagawa, N. Sakaba, and K. Kunitomi, "Spontaneous stabilization of HTGRs without reactor scram and core cooling—Safety demonstration tests using the HTTR: Loss of reactivity control and core cooling," *Nuclear Engineering and Design*, **271**, 379–387 (2014).

[3] Dunfu Shi, "Extension of the Reactor Dynamics Code MGT-3D for Pebblebed and Blocktype High-Temperature-Reactors," PhD Thesis, Forschungszentrum Jülich (2015).

[4] P. Balestra, K. Henry, C. Carlyon, C. English, J. Myer, M. Avramova, A. Epiney, and G. Strydom, "Modular high temperature gas reactor core modeling with RELAP5-3D/PHISICS – Optimization schemes for load following," *Nuclear Engineering and Design*, **362**, 110526 (2020); https://doi.org/10.1016/j.nucengdes.2020.110526., URL `https://www.sciencedirect.com/science/article/pii/S0029549320300212`.

[5] Z. J. Ooi, T. Hua, L. Zou, and R. Hu, "Simulation of the High Temperature Test Facility (HTTF) Core Using the 2D Ring Model with SAM," *Nuclear Science and Engineering*, **0**, *0*, 1 (2022); 10.1080/00295639.2022.2106726., URL `https://doi.org/10.1080/00295639.2022.2106726`.

[6] C. Fiorina, I. Clifford, S. Kelm, and S. Lorenzi, "On the development of multiphysics tools for nuclear reactor analysis based on OpenFOAM®: state of the art, lessons learned and perspectives," *Nuclear Engineering and Design*, **387**, 111604 (2022); https://doi.org/10.1016/j.nucengdes.2021.111604., URL `https://www.sciencedirect.com/science/article/pii/S0029549321005562`.

[7] C. Wang, X. Sun, and P. Sabharwall, "CFD Investigation of MHTGR Natural Circulation and Decay Heat Removal in P-LOFC Accident," *Front. Energy Res.*, **8:129** (2020); 10.3389/fenrg.2020.00129.

[8] C. H. Oh, E. S. Kim, and H. S. Kang, “Natural circulation patterns in the VHTR air-ingress accident and related issues,” *Nuclear Engineering and Design*, **249**, 228 (2012); https://doi.org/10.1016/j.nucengdes.2011.09.031., URL `https://www.sciencedirect.com/science/article/pii/S0029549311008247`, the 8th International Topical Meeting on Nuclear Thermal-Hydraulics, Operation and Safety (NUTHOS-8.

[9] S. Schunert, M. Jaradat, O. Calvin, G. Giudicelli, A. Lindsay, Y. Wang, M. Tano, and S. Walker, “Improvements in High-Temperature Gas-Cooled Reactor Modeling Capabilities in the Pronghorn Code,” INL/RPT-22-69263, Idaho National Laboratory (2022).

[10] W. Xiao, X. Li, P. Li, T. Zhang, and X. Liu, “High-fidelity multi-physics coupling study on advanced heat pipe reactor,” *Computer Physics Communications*, **270**, 108152 (2022); https://doi.org/10.1016/j.cpc.2021.108152., URL `https://www.sciencedirect.com/science/article/pii/S0010465521002642`.

[11] A. Novak, D. Andrs, P. Shriwise, J. Fang, H. Yuan, D. Shaver, E. Merzari, P. Romano, and R. Martineau, “Coupled Monte Carlo and thermal-fluid modeling of high temperature gas reactors using Cardinal,” *Annals of Nuclear Energy*, **177**, 109310 (2022); https://doi.org/10.1016/j.anucene.2022.109310., URL `https://www.sciencedirect.com/science/article/pii/S0306454922003450`.

[12] V. Laboure, J. Ortensi, and A. Hummel, “HTTR 3-D Cross-Section Generation with Serpent and MAMMOTH,” INL/EXT-18-51317, Idaho National Laboratory (2018).

[13] V. Laboure, J. Ortensi, Y. Wang, S. Schunert, F. Gleicher, M. DeHart, and R. Martineau, “Multiphysics Steady-State Simulation of the High Temperature Test Reactor with MAMMOTH, BISON AND RELAP-7,” *M&C 2019*, Portland, OR, USA (2019).

[14] V. Laboure, J. Ortensi, A. Hermosillo, G. Strydom, and P. Balestra, “FY21 Status Report on the ART-GCR CMVB and CNWG International Collaborations,” INL/EXT-21-64241, Idaho National Laboratory (September 2021).

[15] V. M. Labouré, M. A. Lindell, J. Ortensi, G. Strydom, and P. Balestra, “FY22 Status report on the CMVB and CNWG International Collaborations,” INL/RPT-22-68891, Rev000, Idaho National Laboratory (September 2022).

[16] T. P. Freyman and L. C. Charlot, “Modeling of the High Temperature Test Facility PG-26 Transient Using RELAP-7,” INL/EXP-22-68476, Idaho National Laboratory (August 2022)URL `https://inldigitallibrary.inl.gov/sites/sti/sti/Sort_62861.pdf`.

[17] Y. Wang, S. Schunert, J. Ortensi, V. Laboure, M. DeHart, Z. Prince, F. Kong, J. Harter, P. Balestra, and F. Gleicher, “Rattlesnake: A MOOSE-Based Multiphysics Multischeme Radiation Transport Application,” *Nuclear Technology*, **207**, *7*, 1047 (2021); 10.1080/00295450.2020.1843348., URL `https://doi.org/10.1080/00295450.2020.1843348`.

[18] Y. Jung and C. Lee, “PROTEUS-MOC User Manual,” ANL/NE-18/10, Argonne National Laboratory (2018).

[19] R. L. Williamson, J. D. Hales, S. R. Novascone, G. Pastore, K. A. Gamble, B. W. Spencer, W. Jiang, S. A. Pitts, A. Casagranda, D. Schwen, A. X. Zabriskie, A. Toptan, R. Gardner, C. Matthews, W. Liu, and H. Chen, “BISON: A Flexible Code for Advanced Simulation of the Performance of Multiple Nuclear Fuel Forms,” *Nuclear Technology*, 1–27 (2021); 10.1080/00295450.2020.1836940., URL `doi.org/10.1080/00295450.2020.1836940`.

[20] R. A. Berry, J. W. Peterson, H. Zhang, R. C. Martineau, H. Zhao, L. Zou, and D. Andrs, *RELAP-7 Theory Manual*, INL (2014).

[21] R. Hu, L. Zou, G. Hu, D. Nunez, T. Mui, and T. Fei, “SAM Theory Manual,” (2021); 10.2172/1781819., URL `https://www.osti.gov/biblio/1781819`.

[22] A. J. Novak, R. W. Carlsen, S. Schunert, P. Balestra, D. Reger, R. N. Slaybaugh, and R. C. Martineau, “Pronghorn: A Multidimensional Coarse-Mesh Application for Advanced Reactor Thermal Hydraulics,” *Nuclear Technology*, **207**, *7*, 1015 (2021); 10.1080/00295450.2020.1825307., URL `https://doi.org/10.1080/00295450.2020.1825307`.

[23] J. Leppänen, “Serpent– A Continuous-energy Monte Carlo Reactor Physics Burnup Calculation Code.” , VTT Technical Research Centre of Finland (2015).

[24] C. Takasugi, N. Martin, V. Labouré, J. Ortensi, K. Ivanov, and M. Avramova, "Preservation of kinetics parameters generated by Monte Carlo calculations in two-step deterministic calculations," *accepted by EPJ Nuclear Sci. Technol.*; https://doi.org/10.1051/epjn/2022056.

[25] J. Ortensi, B. A. Baker, M. P. Johnson, Y. Wang, V. M. Labouré, S. Schunert, F. N. Gleicher, and M. D. DeHart, "Validation of the Griffin application for TREAT transient modeling and simulation," *Nuclear Engineering and Design*, **385**, 111478 (2021); https://doi.org/10.1016/j.nucengdes.2021.111478., URL https://www.sciencedirect.com/science/article/pii/S0029549321004301.

[26] J. Ortensi, V. Labouré, S. Schunert, and R. Stewart, "Neutronics Enhanced Meshing Operations (NEMO) Users Manual Version 1.0," INL/MIS-20-00730, Idaho National Laboratory (2020).

[27] R. Morris, "CUBIT 15.0 User Documentation," , ETI, UT (2014).

[28] J. Ortensi, Y. Wang, A. Laurier, S. Schunert, A. Hébert, and M. DeHart, "A Newton Solution for the Superhomogenization Method: The PJFNK-SPH," *Annals of Nuclear Energy*, **111**, 579 (January 2018).

[29] V. Labouré, Y. Wang, J. Ortensi, S. Schunert, F. Gleicher, M. DeHart, and R. Martineau, "Hybrid Super Homogenization and Discontinuity Factor Method for Continuous Finite Element Diffusion," *Annals of Nuclear Energy*, **128**, *INL/JOU-18-5106*, 443 (2019); 10.1016/j.anucene.2019.01.003.

[30] Y. Shimazaki, H. Sawahata, M. Shinohara, Y. Yanagida, T. Kawamoto, and S. Takada, "Improvement of neutron startup source handling work by developing new transportation container for high-temperature engineering test reactor (HTTR)," *Journal of Nuclear Science and Technology*, **54:2**, 260 (2017); 10.1080/00223131.2016.1255574.

[31] N. J. Algutifan, S. R. Sherman, and C. W. Alexander, "Comparison of Cf-252 thin-film sources prepared by evaporation or self-transfer," *Applied Radiation and Isotopes*, **96** (2014); 10.1016/j.apradiso.2014.11.025.

[32] "Neutron Sources," Online, https://www.nrc.gov/docs/ML1122/ML11229A704.pdf.

[33] "The fission spectrum," Online, https://indico.cern.ch/event/145296/contributions/1381141/attachments/136909/194258/lecture24.pdf.

[34] J. Bess, N. Fujimoto, B. Dolphin, L. Snoj, and A. Zukeran, "Evaluation of the Start-Up Core Physics Tests at Japan's High Temperature Engineering Test Reactor (Fully-Loaded Core)," INL/EXT-08-14767, Idaho National Laboratory (2009).

[35] D. M. McEligot, G. E. McCreery, R. R. Schultz, J. Lee, P. Hejzlar, P. Stahle, and P. Saha, "Investigation of Fundamental Thermal-Hydraulic Phenomena in Advanced Gas-Cooled Reactors," INL/EXT-06-11801, Idaho National Laboratory (2006).

[36] K. Takamatsu and K. Sawa, "Reactor Kinetics in a Loss-of-Forced-Cooling (LOFC) Test of HTGRs," vol. 2 (2012); 10.1115/ICONE20-POWER2012-54641.

[37] E. Shemon, Y. S. Jung, S. Kumar, Y. Miao, K. Mo, A. Oaks, and S. Richards, "MOOSE Framework Meshing Enhancements to Support Reactor Analysis," techreport, Argonne National Laboratory, ANL/NSE-21/43 (2021); 10.2172/1821454., URL https://www.osti.gov/biblio/1821454.

[38] C. Matthews, V. Laboure, M. DeHart, J. Hansel, D. Andrs, Y. Wang, J. Ortensi, and R. C. Martineau, "Coupled Multiphysics Simulations of Heat Pipe Microreactors Using DireWolf," *Nuclear Technology*, **207**, *7*, 1142 (2021); 10.1080/00295450.2021.1906474., URL https://www.tandfonline.com/doi/abs/10.1080/00295450.2021.1906474.

[39] D. R. Gaston, C. J. Permann, J. W. Peterson, A. E. Slaughter, D. Andrš, Y. Wang, M. P. Short, D. M. Perez, M. R. Tonks, J. Ortensi, L. Zou, and R. C. Martineau, "Physics-based multiscale coupling for full core nuclear reactor simulation," *Annals of Nuclear Energy*, **84**, 45 (2015).

[40] S. Terlizzi and V. Labouré, "Asymptotic Hydrogen Redistribution Analysis in Yttrium Hydride Moderated Heat-pipe-cooled Microreactors using DireWolf," *submitted to Annals of Nuclear Energy* (2022).

[41] R. Siegel and J. Howell, *Thermal Radiation Heat Transfer, Fourth Edition*, Taylor & Francis (2002).

[42] R. Stainsby et al., "Investigation of Local Heat Transfer Phenomena in a Prismatic Modular Reactor Core," NR001/RP/001 R02, AMEC NSS Limited (2009).

[43] J. Ortensi, B. Boer, and A. M. Ougouag, "THETRIS: A micro-scale temperature and gas release model for TRISO fuel," *Nuclear Engineering and Design*, **241**, *12*, 5018 (2011); https://doi.org/10.1016/j.nucengdes.2011.08.072., URL `https://www.sciencedirect.com/science/article/pii/S0029549311007072`, the18th International Conference on Nuclear Engineering (ICONE-18).